



# POLITECNICO MILANO 1863

## Space Propulsion

AY 2023-2024

Professor: Filippo Maggi

## Design of a Liquid Semi-Cryogenic Regenerative Propulsion System for Upper-Stage Applications

Group "Il Problema dei 7 Corpi"

Person Code	Surname	Name
10726898	Juvara	Matteo Giovanni
10631054	Segala	Andrea Giulia
10717230	Beretta	Beatrice
10973642	Separovic	Marko Tomislav
10765536	Mirri	Pietro
10730683	Nuccio	Gabriele
10776736	Natali	Martino

## **Abstract**

This report summarises the design and analysis of a liquid semi-cryogenic regenerative propulsion system for upper-stage applications produced with the use of Additive Manufacturing (AM) technology. The engine uses a blow-down feeding system with LOX-RP1 as a fuel couple.

A preliminary study is performed in the beginning to obtain the design of the feeding system, injection plate, combustion chamber, and nozzle.

Afterwards, a simulation is carried on to analyze the engine's performance throughout the whole firing period and to achieve a more detailed design of the propulsion system .

Lastly, an off-nominal investigation is performed to understand the effect of the AM uncertainties on the injection plate on the overall performances.

# Contents

<b>1</b>	<b>Literature Analysis</b>	<b>7</b>
1.1	Nozzle Losses . . . . .	7
1.2	Additive Manufacturing . . . . .	7
1.2.1	Material Compatibility . . . . .	9
1.3	Blow-Down Feed Systems . . . . .	9
1.3.1	Blow-Down Systems Introduction . . . . .	9
1.3.2	Blow-Down System's Requirements . . . . .	9
1.3.3	Main Concerns on Blow-Down Systems . . . . .	10
1.4	Regenerative Cycle . . . . .	10
<b>2</b>	<b>Engine modelling</b>	<b>11</b>
2.1	Input data . . . . .	11
2.2	Material Selection . . . . .	11
2.2.1	Thrust Chamber Materials . . . . .	11
2.2.2	Tank Materials . . . . .	12
2.2.3	Feeding Pipelines Materials . . . . .	12
2.3	Nozzle . . . . .	12
2.3.1	Expansion Ratio Choice . . . . .	12
2.3.2	General Nozzle Dimensioning Parameters . . . . .	13
2.4	Combustion Chamber . . . . .	13
2.5	Conical Nozzle . . . . .	14
2.6	RAO Nozzle for Maximum Performance . . . . .	14
2.7	Nozzle Losses . . . . .	14
2.8	Injection Plate . . . . .	15
2.9	Feeding Line . . . . .	15
2.10	Insulating Material . . . . .	16
2.11	Tanks . . . . .	17
<b>3</b>	<b>Simulation</b>	<b>18</b>
3.1	Tank Pressures . . . . .	18
3.2	Chamber Pressure and Mass Flow Rates . . . . .	19
3.2.1	Engine Discretization . . . . .	19
3.2.2	Engine Cooling Jacket . . . . .	19
3.2.3	Pressure Losses . . . . .	19
3.2.4	Mass Flow Rate . . . . .	19
3.2.5	Regenerative Cooling . . . . .	20
3.2.6	Chamber Properties and Pressure . . . . .	22
3.3	Thrust . . . . .	22
3.4	Remaining Propellant Mass . . . . .	22
<b>4</b>	<b>Results and Comments of the Nominal Design</b>	<b>22</b>
4.1	Nozzle . . . . .	22
4.1.1	Expansion Ratio Choice [2.3.1] . . . . .	22
4.1.2	General Nozzle Dimensioning Parameters [2.3.2] . . . . .	23
4.2	Combustion Chamber [2.4] . . . . .	23
4.3	Conical Nozzle [2.5] . . . . .	24
4.4	RAO Nozzle [2.6] . . . . .	24
4.5	Nozzle Losses [2.7] . . . . .	24
4.6	Injectors [2.8] . . . . .	25
4.7	Feeding Line [2.9] . . . . .	25
4.8	Insulating Material [2.10] . . . . .	25
4.9	Tanks [2.11] . . . . .	26

<b>5</b>	<b>Results and Comments of the Simulation</b>	<b>26</b>
5.1	Re-Sizing . . . . .	26
5.2	Results . . . . .	26
5.3	Off-Nominal Condition . . . . .	28
5.4	Limitations of the model . . . . .	30
<b>6</b>	<b>Conclusion</b>	<b>31</b>
<b>A</b>	<b>Appendix: Literature Analysis</b>	<b>35</b>
<b>B</b>	<b>Appendix: Engine Modelling</b>	<b>36</b>
<b>C</b>	<b>Appendix: Results and Comments</b>	<b>40</b>

## Acronyms

**AISI** American Iron and Steel Institute. 12

**AM** Additive Manufacturing. 2, 7–10, 12, 31

**AOCS** Attitude and Orbital Control System. 17

**DED** Direct Energy Deposition. 8, 32

**DMLS** direct metal laser sintering. 8

**EPC** Etage Principal Cryotechnique. 12

**LOX** Liquid Oxygen. 2, 12, 17

**LPBF** Laser powder bed fusion. 8, 9, 31

**MSFC** Marshall Space Flight Center. 9

**NASA** National Aeronautics and Space Administration. 9, 33

**PBF** Powder Bed Fusion. 8, 31

**RP1** Rocket Propellant 1. 2, 17

**SLM** selective laser melting. 8

## Symbols List

$v$	velocity
$M$	mach number
$t$	time
$F$	force
$m$	mass
$\dot{m}$	mass flow rate
$\epsilon$	nozzle expansion ratio
$\epsilon_c$	contraction ratio
$\gamma$	specific heat ratio
$P$	pressure
$c^*$	characteristic velocity
$c_t$	thrust coefficient
$M_m$	molar mass
$A$	area
$D$	diameter
$I_{sp}$	specific impulse
$V$	volume
$\rho$	density
$L$	length
$L^*$	characteristic length
$\alpha_{conv}$	convergent angle
$\alpha_{div}$	divergent angle
$\theta$	Rao angle
$f$	friction coefficient
$K$	resistance coefficient
$Cd$	discharge coefficient
$T$	Thrust
$T$	Temperature
$Re$	Reynolds
$Nu$	Nusselt
$Gr$	Grashof
$Ra$	Rayleigh
$Pr$	Prandtl
$Nu$	Nusselt number
$k_t$	curvature
$\lambda$	2D loss coefficient
$\mu$	dynamic viscosity
$k$	thermal conductivity
$c_p$	specific heat
$q$	thermal flux
$r$	radius
$h$	convection coefficient
$OF$	oxidizer to fuel ratio
$t$	thickness
$\sigma$	ultimate tensile strength

# 1 Literature Analysis

In this section a brief analysis of the literature has been carried out. In particular the topics of **Nozzle Losses**, **Additive Manufacturing**, and **Blow-Down Systems** are explored in further detail.

## 1.1 Nozzle Losses

The losses that occur within the nozzle are crucial to understand how to size and design the engine properly. These losses depend on several factors such as the propellant couple and the nozzle type [31]. Due to the losses, some of the internal energy of the real nozzle flow is unavailable for conversion into kinetic energy at the exhaust [28]. Below are explained some of the possible losses that can occur in a vacuum environment:

- **Divergence Losses:** the exit velocity vector should be as parallel as possible to the nozzle axis in order to provide the best performance possible. The perpendicular component of the vector is indeed not useful to the production of thrust, causing a drop in the thrust level if not properly aligned. In order to reduce the effect of these losses, more complex contoured nozzles are used, the most implemented of which is the RAO nozzle [30], which is based on the assumption of inviscid, isentropic flow. This method allows the optimization of the rocket nozzle contour for a given length or expansion ratio to achieve optimum thrust, minimizing the divergence losses.
- **Viscosity Losses:** Real nozzles develop thin viscous boundary layers adjacent to their inner walls, where gas velocities are much lower than in the free-stream region of the nozzle. This layer is cooler than the free flow of the nozzle due to heat transfer mechanics with the wall. These low velocities reduce the average exhaust gas exit velocity by a percentage between 0.5% and 1.5%, resulting in an apparent shrinkage of the flow at the nozzle exit, which translates into decreased mass flow and lower thrust.
- **Pressure Losses:** low contraction ratios  $A_l/A_t$  cause pressure losses and slightly reduce thrust and exhaust velocity.
- **Gas Chemical Properties Losses:** Chemical reactions within nozzle flows can alter the gas composition, properties, and temperatures, resulting in losses of up to 0.5%. Also, non-uniform gas compositions, resulting from incomplete combustion and mixing, can cause performance loss. Lastly, real gas properties may alter the gas composition, resulting in performance losses ranging from 0.2% to 0.7%.
- **Throat Erosion:** The throat's diameter increases in time, due to erosion in that area, especially if using uncooled nozzle materials. This increment results in a drop of chamber pressure and thrust.
- **Transient Losses:** During transient performance, such as starts, stops, or pulsing modes, chamber pressures and overall performances are generally lower. Additionally, if unstable combustion or flow oscillations are present, small losses may occur.
- **Heat Transfer Losses:** Losses due to heat transfer from the main flow depend mainly on the size of the nozzle and the cooled layer along its walls.
- **Multi-Phase Flow Losses:** The gaseous working fluid may contain small liquid droplets and solid particles entrained in the flow. These could lead to excessive heating of the gas during nozzle expansion, which results in losses that influence the overall performance of the system. These particles can interact with the walls of the nozzle itself or with other components causing erosion or structural damage.

## 1.2 Additive Manufacturing

The Additive Manufacturing (AM) of metals is a processing technology that defines a layer-by-layer fabrication method to form three-dimensional shapes as opposed to machining (also known as subtracting manufacturing) or joining multiple parts. This technology has significantly matured over the last decade and a significant portion of AM development is focused on liquid rocket engine applications.

Advantages	Disadvantages
Rapid production	Not perfect surface finish
Increasing performances	Design limitations
Reductions in overall lifecycle costs	Scale limitation
Complex shape manufacturing	Residual thermal stress

Table 1: Pros and Cons of AM [32][22][18]

In Figure 12 are reported the typical Additive Manufacturing processes, the most important are:

- **Powder Bed Fusion (PBF)**, which uses a layer-by-layer powder-bed approach in which the desired component features are sintered and subsequently solidified using a laser. This technology guarantees the highest resolution for AM but the dimension scale is very limited [32];
- **Direct Energy Deposition (DED)**, which is a 3D printing method that uses a focused energy source, such as a plasma arc, a laser, or an electron beam to melt a material which is simultaneously deposited by a nozzle. These additive deposition technologies have been demonstrated to provide faster near-net shape fabrication for larger components [16];

In this project, the focus will be on PBF, in particular on Laser powder bed fusion (LPBF), also known as selective laser melting (SLM) or direct metal laser sintering (DMLS), which is one of the most mature AM technologies.

Despite the fact that LPBF generally guarantees high-resolution components, the roughness and the intrinsic limitations of this technology must be taken into account during the design phase.

The principal design issues are [18]:

- **Wall Thickness**; it is important to ensure that the wall thickness of the produced parts is neither too thin or too thick, as this can result in either a delicate print or a build-up of internal stresses, which leads to cracking. A first approximation of a minimum wall thickness may be 0.4 mm;
- **Overhangs**; the maximum length of an unsupported horizontal overhang is 0.5 mm. In addition to that value, the overhangs will require support structures to prevent them from collapsing during the production process;
- **Channels and Holes**; the minimum diameter for most powder-bed processes is 0.4 mm and hollow metal parts require escape holes to remove any un-melted powder;

The tolerances of the components depend on the material selected and the specific machine used for printing, a general value could be estimated around  $\pm 0.5\%$  with a lower limit of  $\pm 0.5$  mm [1].

Looking at EOS and Concept Laser 3D printing equipment, the typical tolerance ranges of  $\pm 0.1$  mm to  $\pm 0.2$  mm are expected and generally achieved [7].

The most relevant issue for SLM, and in general to all AM, is the roughness. Components cannot be printed with the same accuracy as they would have if manufactured by precision turning and milling [42]. Furthermore, the part orientation must be taken into account as downward and upward-facing surfaces will have a different surface roughness and down-skins tend to have an inferior surface finish [18].

The roughness depends on the material selected and the specific machine resolution, typical values are up to 20  $\mu\text{m}$ . In Table 2 are reported some examples of available levels of surface finish.

Material	Inconel 718	GRCOP-42	C-103	Ni-718
<b>Roughness</b> [ $\mu\text{m}$ ]	5.7 to 7.5	8 to 10	8 to 12	around 5
<b>Company</b>	Protolabs	3D Systems	3D Systems	3D Systems

Table 2: Roughness [3][4][11][12]

Post-processing methods like vibratory machines and hand sanding are used in some applications where a higher surface finish is required [17].



### 1.2.1 Material Compatibility

AM process has distinct sets of compatible materials. Compatibility generally depends on:

- **Feedstock Manufacturing:** the metal must be able to be processed into a feedstock of suitable type and quality for the AM process;
- **Printability:** the feedstock material must behave acceptably during the manufacturing process;
- **As-Printed State:** the final quality and state (hardness, grain size, etc.) of the printed material must meet requirements;

Powder-based metal AM processes often have stringent requirements on the powder’s morphology, ductility, absorption, and reflectivity [19].

NASA Marshall Space Flight Center (MSFC) has been involved in numerous studies on LPBF in liquid rocket engine component design, development, and testing since 2010, in Ref. [32]11 a numerous example of materials can be found.

## 1.3 Blow-Down Feed Systems

### 1.3.1 Blow-Down Systems Introduction

One of the more prevalent configurations in the field of rocket propulsion systems is the blow-down feed system, which uses pressurised gas to drive propellants into the combustion chamber. This system operates by forcing propellants into the combustion chamber using the stored energy obtained from a pressurised inert gas.

Blow-down feed systems are often chosen for systems where simplicity, reliability, and cost-effectiveness are preferred over other features. Their straightforward design and operational mechanism make them favorable for applications where intricate pressurization systems or complex plumbing arrangements are not feasible or necessary such as small-scale rocket engines, experimental setups, and particular cases of maneuvering thrusters.

The main difference of a blow-down system with respect to other feed systems is larger and heavier propellant tanks with a large ullage volume (30–60 %), as these are meant to store not only the propellants but also the pressurizing gas at an initial maximum propellant tank pressure. In a blow-down system, there is no need for a separate high-pressure gas tank and no pressure regulator as the pressure decreases with the propellant mass inside the tank. The expansion of the pressurizing gas in the tanks provides enough energy for the complete expulsion of the propellants.[31]

Advantages	Disadvantages
Simpler system Less pressurizing gas and inert mass No use of high-pressure pressurizing gas tanks	Thrust decreases with the burn duration Higher residual propellant Lower specific impulse at the end of the burning

### 1.3.2 Blow-Down System’s Requirements

One of the key requirements of the system is propellant temperature.

In a blow-down system, it is desirable to avoid large temperature gradients between fuel and oxidizer to minimize residuals which could adversely affect thruster performance and thermal control. Results of studies and testing have shown that a 278-305 K temperature range is generally acceptable. Below the minimum value, there is increased concern regarding oxidizer flow decay, whereas, above the maximum value, performance losses become significant in some thrusters.

Gas ingestion requirements may also be affected by the initial launch configuration, as the feed-line region may initially contain only pressurizing gas or consist of a soft load of a gas/liquid mixture. There are also some feed system effects that must be taken into account when identifying thruster requirements. Water-hammer analyses, and possibly testing, should be conducted over the range of inlet pressures and duty cycle types expected for the mission. Important variables include line sizes, plumbing layout, and

thruster valve response. Operating and proof pressure requirements can be influenced as well by the presence of upstream isolation valves in the system.

The determination of the operating pressure envelope is one of the key tasks in the evaluation and development of any blow-down system since it affects analyses and testing in other important areas such as performance, stability, and thermal control. [33]

### 1.3.3 Main Concerns on Blow-Down Systems

In the following section the main concerns when implementing a blow-down architecture are explored [33]:

- **Performance:** since a blow-down system operates over a wide range of pressures and mixture ratios large variations in performance may occur. Various tests have been performed on multiple thrusters using blow-down systems and the results showed that significant reductions in performance begin to show up as inlet pressure drops below 1-1.4 Mpa; while large mixture ratio excursions do not result in significant performance penalties, but does result in increased chamber temperature.
- **System Lifetime:** the life of thrusters is influenced by temperature, time, and number of thermal cycles. Both nozzle and injector efficiencies generally improve with higher chamber pressure, however since chamber heat flux and operating wall temperature also increase with pressure, thus resulting in coating degradation and reduced lifetime. One approach is to reduce the efficiency of existing designs in order to achieve lower wall temperatures. Another approach is the use of a cavitating venturi to reduce the total flow rate range. This may prove practical, but potential disadvantages include unacceptable pressure losses and possible effects due to propellant outgassing.
- **Ignition Spikes:** the potential for damaging ignition spikes exists for bipropellant thrusters. The most significant result from thruster testing was that ignition spike amplitudes were not greatly influenced by inlet pressure. It appears that implementing blow-down systems does not create adverse ignition spike conditions.
- **High-Frequency Stability:** high-frequency pressure oscillations are usually associated with one or more of the acoustic vibration modes within the chamber. Such vibrational motions are damped by viscous effects in the chamber and by acoustic resonator cavities built into the injector face. Data evaluated revealed a higher than expected average chamber pressure 1.13 vs 0.99 MPa during the instability. Inspection of the thruster also showed damage to the coating inside the chamber. Previous testing indicate that high-frequency instabilities are more likely at high inlet pressures.
- **Low-Frequency Stability:** chugging is a low-frequency thruster instability in which chamber pressure oscillations are coupled to feed system hydraulics. Blow-down operation may influence the onset of chugging and combustion time lags that are affected by chamber pressure and mixture ratio. The concerns raised by chugging include the possibility of excessive thrust chamber heating through increased heat-transfer rates, effects on thruster performance and efficiency, induced mechanical vibrations, feed system effects on other thrusters and components, and the possibility of triggering high-frequency instability. It is seen that thruster stability increases with lower mixture ratio and higher inlet pressure. If chug stability problems are found, potential fixes include decreasing thruster design point mixture ratio, thruster injector modifications, changes in the tank pressure operating envelope, and adding damping devices to the feed system.

## 1.4 Regenerative Cycle

A regenerative cycle provides many advantages to the design of the engine. The propellant is used to cool the engine walls before it is combusted, this not only prevents the engine from overheating but also increases the thermal efficiency by preheating the propellant. This comes at the cost of an added complexity in the engine design, however AM lends itself to produce this type of shapes and hollow channels. Also there is an increase in the fuel pressure drop and a risk of the fuel overheating.

## 2 Engine modelling

### 2.1 Input data

The input data from which we started our analysis where the following:

Table 3: Input data

From Project Requests	From Rocket Propulsion Element [31]
<ul style="list-style-type: none"> <li>• <b>LOX-RP1</b> - Liquid semi-cryogenic propulsion to be operated in vacuum;</li> <li>• <math>T_i</math> - Initial thrust (1000 N);</li> <li>• <math>P_{cc,i}</math> - Initial combustion chamber pressure (50 bar);</li> <li>• <math>P_{cc,f}</math> - Minimum combustion chamber pressure (20 bar);</li> <li>• <b>Space allocated for propulsion system:</b> Cylinder of 2 m length and 1 m diameter. 80% of the volume is tanks + combustion chamber up to the convergent, 20% is empty spaces.</li> <li>• <b>Blow-down:</b> Feeding rocket engine design;</li> <li>• <b>Additive manufacturing:</b> the manufacturing process for the injector and thrust chamber;</li> </ul>	<ul style="list-style-type: none"> <li>• <math>OF</math> - Oxidizer to fuel ratio (maximum performance condition);</li> <li>• <math>M_m</math> - Molar mass (maximum performance condition);</li> <li>• <math>\gamma</math> - Specific heat ratio of the combustion chamber mixture (maximum performance condition);</li> </ul>

Regenerative cooling, employing RP-1, has been incorporated into the engine design.

### 2.2 Material Selection

#### 2.2.1 Thrust Chamber Materials

Following the previous literature analysis on additive manufacturing in subsection 1.2 and the preliminary design, the manufacturing process chosen for the thrust chamber is direct metal laser sintering additive manufacturing.

The materials were compared by looking at printability, previous applications, and chemical, thermal, and mechanical properties; and three metal alloys have been selected:

- **Inconel-718:** is a high strength, corrosion resistant nickel-chromium super-alloy.
- **GRCOP-42:** is a copper alloy specifically designed for high-temperature, high-thermal transfer applications where high strength and creep properties are also a hard requirement.
- **C-103:** is a niobium alloy with hafnium and titanium alloying elements. It is a refractory material specifically designed for high-temperature and high-corrosive operating applications.

Material	Inconel-718 [11] [14]	GRCOP-42 [26][20][4]	C-103 [3][13]
Density [kg m <sup>-3</sup> ]	8190	8790	8870
Roughness [μm]	5.7 to 7.5	8 to 10	8 to 12
Thermal Conductivity [W m <sup>-1</sup> K <sup>-1</sup> ]	11.4	344	41.9
Specific Heat [J g <sup>-1</sup> K <sup>-1</sup> ]	0.435	0.520	0.340
Ultimate Tensile Strength [MPa]	960 to 1240	360	574
Yield Strength $R_{p0.2\%}$ [MPa]	600 to 940	195	461
Operating Temperature [°C]	up to 700	up to 750	up to 1500

Table 4: Material Properties at Standard Temperature

Thanks to the Additive Manufacturing process the combustion chamber, the nozzle and the injection plate can be printed as a single component providing several advantages such as a reduction in cost, weight, and complexity [36].

Although the GRCOP-42 alloy has a higher thermal conductivity, an optimal characteristic for the cooling of the component, the material chosen is the C-103 since it is characterized by better mechanical properties and a significantly higher operating temperature with respect to GRCOP-42 and Inconel. Furthermore, the Space X engine, Kestrel, used for the Falcon-1 upper stage until 2009, was made by a niobium alloy and operated with LOX/RP1 [40].

### 2.2.2 Tank Materials

For the tank materials some critical factors have to be considered when choosing the appropriate material. The main factors taken into account are:

- The resistance to corrosivity, as Liquid Oxygen is a very corrosive oxidizer;
- The density of the material, to lower the mass of the tanks as much as possible;
- The tensile strength of the material, to be able to withstand the pressures in the tank with a 100% margin.

The choice of the material fell on aluminium 7020 T-6 alloy (UNS A97020). This particular alloy has a great resistance to corrosivity and the ability to operate without losing physical properties at cryogenic temperatures. Furthermore this alloy has a very high tensile strength ( $\sigma = 350\text{MPa}$ ) with respect to other alloys used for these applications, such as Al 2219 or Al 2319, and still maintains a low density ( $2780\text{ kg/m}^3$ ), typical of aluminium materials [6]. Finally, this alloy has a very successful track record for the storage of cryogenic propellants, such as in the Etage Principal Cryotechnique (EPC) of the Ariane V launchers, which assures it's reliability in critical upper-stages of rocket launchers. [5]

### 2.2.3 Feeding Pipelines Materials

The material selection for the feed pipes was easier as the only factors to be considered were the resistance to corrosion, the Liquid Oxygen, and the tensile strength, which should be enough to withstand the pressure of the propellants. Since it was decided to use pipes with a diameter of 1/2 in (6.25 mm) the mass of the pipes is negligible with respect to other masses of the system, for this reason higher density materials may be used. In particular it was chosen to use the steel AISI 316L. This alloy is widely used for the management of cryogenic propellants. This is due to the high operating temperature range of the material and its excellent ductility and weldability. Furthermore, alloy 316L has a higher resistance to corrosion with respect to other similar alloys, such as AISI 304 or AISI 310. [2]

## 2.3 Nozzle

### 2.3.1 Expansion Ratio Choice

The primary consideration in designing the nozzle, based on initial input parameters, is determining the expansion ratio. The engine is tailored for upper stage operation, meeting the prescribed thrust requirement, vacuum operational demands and aligning with the selected propellant type. For missions involving upper stage operations, expansion ratios typically range from 50 to 200. To initiate the design process, a reference expansion ratio of  $\epsilon = 100$ . Subsequently, the design process starts based on this reference expansion ratio. The obtained values of propellant masses and thrust chamber mass were used as a reference for the choice of the optimal expansion ratio. This optimization process evaluates changes in thrust chamber mass and specific impulse. An 85% propellant mass ratio (typical for upper stages) was applied to obtain the total mass calculated. The goal is computing the maximum increase of  $\Delta v$ . The  $\Delta v$  is computed with the Tsiolkovsky equation, as a function of the varying  $I_{sp}$  and  $\Delta m$  from the

reference thrust chamber mass at  $\epsilon=100$ :

$$\Delta m = m_{tc} - m_{tc100} \quad \Delta v = I_{sp} \cdot g_0 \cdot \log \left( \frac{m_0 + \Delta m}{m_f + \Delta m} \right) \quad (1)$$

The chosen epsilon is the one that ensures the maximum  $\Delta v$  increase. The admissibility of the total length of the thrust chamber and the exit diameter is then verified, taking into account the permissible dimensions for additive manufacturing.

### 2.3.2 General Nozzle Dimensioning Parameters

The initial assumption for nozzle computation is isentropic expansion, which is a simplification because it offers several advantages. Firstly, it simplifies the computation of required parameters using straightforward equations, making it highly beneficial for preliminary design. Additionally, any deviations from real performance can be accounted for by calculating losses, notably viscosity and divergence losses. The first parameter to compute is the exit pressure:

$$\frac{1}{\epsilon} = \left( \frac{\gamma + 1}{2} \right)^{\frac{1}{\gamma-1}} \left( \frac{P_e}{P_{cc.in}} \right)^{\frac{1}{\gamma}} \sqrt{\frac{\gamma + 1}{\gamma - 1} \left( 1 - \left( \frac{P_e}{P_{cc.in}} \right)^{\frac{\gamma-1}{\gamma}} \right)} \quad (2)$$

From this equation  $P_e$  is obtained.

Then, the values of characteristic velocity and thrust coefficient are computed, considering  $P_a=0$  (vacuum condition).

$$c^* = \sqrt{\frac{\frac{RT_{cc1}}{M_m}}{\gamma \left( \frac{2}{\gamma+1} \right)^{\frac{\gamma+1}{\gamma-1}}}} \quad c_t = \sqrt{\frac{2\gamma^2}{\gamma-1} \left( \frac{2}{\gamma+1} \right)^{\frac{\gamma+1}{\gamma-1}} \left( 1 - \left( \frac{P_e}{P_{cc.in}} \right)^{\frac{\gamma-1}{\gamma}} \right)} + \frac{P_e - P_a}{P_{cc.in}} \epsilon \quad (3)$$

The area of the throat is determined from the definition of  $c^*$  and the exit area. Subsequently, the respective diameters are derived from these values.

$$A_t = \frac{T_{in}}{P_{cc.in} \cdot c_t} \quad A_e = \epsilon \cdot A_t \quad (4)$$

The last value to compute are the specific impulse, the mass flow rate and the exit velocity, with the following formulas:

$$I_{sp} = \frac{c_t \cdot c^*}{g_0} \quad \dot{m}_{flow} = \frac{T_{in}}{I_{sp} \cdot g_0} \quad v_e = \sqrt{2 \left( \frac{\gamma}{\gamma-1} \frac{R}{M_m} T_{cc1} \left( 1 - \left( \frac{P_e}{P_{cc.in}} \right)^{\frac{\gamma-1}{\gamma}} \right) \right)} \quad (5)$$

## 2.4 Combustion Chamber

To design the combustion chamber the starting point is the characteristic length for the decided fuel and oxidizers. From [31] the value for the couple LOX/RP-1 is obtained. Then the combustion chamber volume is determined as:

$$V_{cc} = L^* \cdot A_t \quad (6)$$

To fully define the combustion chamber the contraction ratio also need to be fixed.  $\epsilon_c$  is obtained from an experimental formula found in [38], based on the interpolation of contraction ratio in flown engines. From that the combustion chamber area and therefore the diameter is computed.

$$\epsilon_c = [8 \cdot (D_t)^{-0.6} + 1.25] \quad A_{cc} = \epsilon_c \cdot A_t \quad (7)$$

Finally from the volume and area of the combustion chamber the length is derived, considering a cylindrical shape. The thickness of the combustion chamber is not determined only based on resisting the pressure differential  $\Delta P$ . Indeed, the presence of a cooling jacket results in a minimal pressure differential between the interior of the combustion chamber and the fluid passing through it. The primary consideration for dimensioning the chamber is its ability to withstand thermal stresses induced by the cooling jacket.

## 2.5 Conical Nozzle

The conical nozzle is defined to compute the RAO, which ensures better performance. To accomplish this, the half-angles of the cone are defined as  $\alpha_{conv} = 45^\circ$   $\alpha_{div} = 15^\circ$ . [28] The length of the convergent and divergent nozzle sections are computed as:

$$L_c = \frac{1}{2} (D_{cc} - D_t) \cdot \tan(\alpha_{conv}) \quad L_d = \frac{1}{2} (D_e - D_t) \cdot \tan(\alpha_{div}) \quad (8)$$

## 2.6 RAO Nozzle for Maximum Performance

The RAO nozzle is optimized for maximum performance by ensuring that both the divergent and convergent lengths match those of the conical nozzle (therefore a 100% length for the divergent in the graphs). Subsequently, the RAO angles are extrapolated from the graph provided in the section B of appendix Figure 14. The total length of the nozzle is determined by summing the convergent and divergent lengths.

## 2.7 Nozzle Losses

Nozzle losses are determined to compute the real value of thrust, considering the divergence and viscosity losses:

- Divergence losses: due to the imperfect alignment of the outflow at the nozzle exit, the actual thrust value is diminished. This reduction is better mitigated when using the RAO nozzle. The real thrust is computed using the parameter  $\lambda$ , which is a function of the angles  $\alpha_{div}$  and  $\theta_f$  (exit RAO half-angle), and is defined as follows:

$$\lambda = \frac{1}{2} \left( 1 + \cos \left( \frac{\alpha_{div} + \theta_{fin}}{2} \right) \right) \quad (9)$$

- Viscosity losses: due to the boundary layer's presence, leading to apparent shrinkage at throat cross section. This phenomenon contributes to a decrease in the mass flow rate and consequently reduces the thrust. In order to compute them it is necessary to evaluate the  $c_d$  which is the ratio between the real and the ideal mass flow rate. Starting from the throat radius, curvature ( $k_t = 1.5r_{throat}$  for RAO) and Reynolds the  $c_d$  is obtained as:

$$Re_{mod} = \sqrt{\frac{R_t}{k_t}} \cdot Re_t \quad (\text{Modified Reynolds}) \quad (10)$$

$$C_d = 1 - \left( \frac{\gamma + 1}{2} \right)^{3/4} \left( 3.266 - \frac{2.128}{\gamma + 1} \right) Re_{mod}^{-1/2} + 0.9428 \left( \frac{\gamma - 1}{\sqrt{\gamma + 1}} \right) Re_{mod}^{-1} \quad (11)$$

From these losses it is first computed the real mass flow rate.

$$\dot{m}_{flowReal} = \dot{m}_{flowIdeal} \cdot C_d \quad (12)$$

Using the  $\dot{m}_{flowReal}$  the thrust is obtained considering the viscosity losses. Multiplying the dynamic part of the thrust by the  $\lambda$  coefficient also the 2D losses are taken into account. Therefore the real thrust is computed as follows:

$$T_{real} = \lambda \cdot \dot{m}_{flowReal} \cdot v_e + A_e \cdot (P_e - P_a) \quad (13)$$

Other types of losses, described in subsection 1.1, were neglected for the following reasons:

- Chamber pressure losses due to a small contraction ratio are negligible since they become noticeable only for  $\epsilon_c < 4$  (the computed  $\epsilon_c$  for this design is 9).
- Unsteady combustion and flow oscillations may result in small losses, which are better evaluated with experimental data.

- Multi-phase losses are disregarded as they predominantly affect hybrid or solid rockets due to the presence of solid particles in the flow. In bipropellant liquid engines, the primary source of such losses is the existence of small liquid droplets. However, the selection of an injector optimized for mixing ("unlike" triplet impinging), along with the high combustion chamber pressure, significantly restricts their occurrence.
- Losses due to chemical reactions occurring within the nozzle flow, which can alter the mixture composition, as well as non-uniform gas composition and real gas property losses, can be estimated. However, as the simulation model employs the frozen chemistry expansion model, which already underestimates real performance, these additional losses were not incorporated.
- Losses in transient performance are not considered since the engine is preliminary designed in a steady state.
- Gradual erosion of the throat region is not a concern as there is no ablative material, and the cooling jacket provides sufficient protection.

Finally the real specific impulse can be computed, which reflects a little decrease in the performance compared to the ideals one:

$$I_{\text{real}} = \frac{T_{\text{real\_RAO}}}{\dot{m}_{\text{flowReal}} \cdot g_0} \quad (14)$$

## 2.8 Injection Plate

The selected injector's type is an "unlike" triplet impinging with an O-F-O configuration because [35][21]:

- It allows a high mixing, which compensates for the lower inherent volatility of the fuel;
- It does not need a large number of smaller holes to satisfy the vaporization requirements for good performance;
- It helps when there is a mismatch in the fuel and oxidizer stream momentum, which may result in an unfavorable resultant angle
- Impinging jet designs are quite popular when the oxidizer is liquid oxygen;

This configuration's main drawback is the minor stability with respect to the other common injector designs. The material selection is explained in the section 2.2.1.

The orifices are sharp-edged with  $D_{inj} = 1.2\text{ mm}$ , with a tabulated discharge coefficient  $c_D = 0.65$ [31]. The LOX injectors are inclined by 30 deg with a symmetric configuration. Knowing the diameter of the combustion chamber, the decision on the number of injectors was made, 4 for the fuel and 8 for the oxidizer. After computing the total injection area, the analysis terminates with the evaluation of the oxidizer and fuel injectors velocity that derives after computing the pressure drops.

$$\Delta P_{inj} = \frac{\dot{m}_{flow}}{2(c_D A_{inj})^2 \rho_{prop}} \quad v_{flow} = \sqrt{\frac{2\Delta P}{\rho k_{inj}}} \quad (15)$$

where  $k_{inj} = \frac{1}{c_D^2}$ .

## 2.9 Feeding Line

The bi-propellant feeding system is composed of a fuel and an oxidizer tanks containing both also the pressurizing gas. The selected pressurant gas is He, commonly used in blow-down systems and mostly adopted in similar applications. To proceed, a pressure cascade analysis is performed in order to size the volume and mass of the propellant and pressurizer starting from the combustion chamber pressure and considering pressure drop contributes from injector plate, feeding lines, valves, dynamic flow, entrance in the pipes and cooling cycle.

$$P_{ox,tank} = P_{CC} + \Delta P_{inj} + \Delta P_{feed} + \Delta P_{check\ valve} + \Delta P_{dyn} + \Delta P_{entry} + \Delta P_{sol\ valve} \quad (16)$$

The pressure drops in the fuel line were calculated using the same equation but with the inclusion of an additive term. In fact the RP-1 was also used for the regenerative cooling system and so another distributed pressure drop happen. This last value was computed by considering an average value for the diameter of the cooling channel  $D_{channel} = 5$  mm.

The pipelines fed system was designed in an original way, by positioning the tanks in a tandem configuration, the optimization of the used space became crucial. To make this feasible, the oxidizer pipeline passes through the fuel tank; as expected this solution requires some precautions as the LOX storage temperature is way smaller than the RP-1. In the following paragraphs, this will be explained in detail. The diameter of the pipelines was selected regarding the standards values for the evaluated mass flow rate,  $D_{pipes} = 1/4$  " while the length differs with respect to the propellant by a first evaluation of the tanks length and the available space:  $L_{pipe,ox} = 0.74$  m and  $L_{pipe,f} = 0.38$  m.

$$\Delta P_{feed} = f_D \frac{\rho L}{2D} v_{feed}^2 \quad (17)$$

where  $f_D$  is the Darcy friction factor obtained with the Colebrook - White equation [43]:

$$\frac{1}{\sqrt{\lambda}} = -2 \log \left( \frac{\epsilon/D}{3.71} + \frac{2.51}{Re\sqrt{\lambda}} \right) \quad (18)$$

knowing the Reynolds number and the relative roughness which is 0.032%.

Among the three types of concentrated pressure drops the one related to the solenoid valve is found by considering a flow coefficient of  $K_v = 1.1$ .

The last Pressure drop term that was analyzed is the annular pressure drop in the regenerative cooling line around the engine. The cooling system will be further analyzed in 3. To compute this term it was considered a distributed loss with a hydraulic diameter of 5 mm. The right computation requires a correction factor for concentric channels, this was obtained from the the diameter of the considered cylinder and is equal to 0.66718. By just multiplying this factor with the diameter and with the Reynolds number in the channel, the drop is easily computed.

## 2.10 Insulating Material

In order to save the biggest amount of space possible and to maintain the system's stability, without compromising the functionality of the designed component, it has been decided to make the oxidizer's feeding line pass through the fuel's tank, as it was done in the Saturn V architecture [39]. Therefore it was necessary to size a layer of an insulating material for the tubes containing the Liquid oxygen. Selecting and sizing an insulating material with high efficiency is crucial to maintain the desired temperature of the LOX and prevent cavitation phenomena. To proceed with the sizing, some data was found in the literature or assumed:

	<b>RP-1</b>	<b>LOX</b>
$k[W\ m^{-1}\ K^{-1}]$	0.115	0.09
$T[K]$	293.15	120
$\mu[Pa\ s]$	0.00075	0.000103
$\rho[kg\ m^{-3}]$	830	980
$c_P[J\ kg^{-1}\ K^{-1}]$	1884.1	2302.7

Table 5: Insulant

While the conductivity coefficient for the tube is  $k_T = 15W\ m^{-1}\ K$  and the one for the chosen insulant is  $k_{is} = 0.035\ W\ m^{-1}\ K^{-1}$  [10]

The thermal flux passing through the tube per unit length is:

$$q = K(T_{ox} - T_{fuel,tank}) \quad (19)$$



Where  $K$  is the total transmittance's coefficient for unit length, which takes into account the thermal conductivity heat exchange between the tube and the insulation, between the insulation and the surrounding environment, and the convective heat exchange of the internal wall of the tube and the external wall of the insulant. To compute the Nusselt number of the internal flow, it was considered as a forced convection phenomenon while for the external flow of fuel, it was chosen to assume natural convection as the velocity of the fuel in the tank is negligible. After computing the Grashof, Prandtl, and then Rayleigh numbers of the fuel, the Nusselt number is found with the law adopted for natural convection in cylindrical tubes[27]:

$$Nu_f = 5.75 + 0.75(Ra_e/f(Pr))^{0.252} \quad (20)$$

where  $f(Pr)$  is a function of the Prandtl number:

$$f(Pr) = \left(1 + \left(\frac{0.49}{Pr_f}\right)^{9/16}\right)^{16/9}; \quad (21)$$

The sizing aim is establishing the thickness of the insulant, afterwards the total transmittance  $K$  in dependence of the insulant radius is:

$$K = \frac{2\pi}{\frac{1}{h_{ox}r_{ox}} + \frac{\log(r_e/r_i)}{k_t} + \frac{\log(r_{is}/r_i)}{k_{is}} + \frac{1}{h_f r_{is}}} \quad (22)$$

and then impose that the LOX maximum temperature ( $T_m = 133K$ ) is not reached, as it is the boiling point at the minimum operating pressure of 20 bar, with:

$$T_{LOX} + K \frac{T_{RP1} - T_{LOX}}{2\pi r_{is} h_e} \leq T_m \quad (23)$$

Through an iterative process, it was possible to obtain the minimum radius of the insulation and, subtracting the external radius of the tube, the minimum thickness of the insulating material was obtained[27].

## 2.11 Tanks

The architecture for the tanks position was selected as the best possible to maximize the available volume and to avoid problems as cavitation and other unwanted heating of the cryogenic oxidizer. Two cylindrical tanks were selected with the maximum diameter available, leaving a margin of 15 mm for eventual filling ports.

The tandem position chosen sees the oxidizer tank arranged above the fuel tank in order to guarantee space between the combustion chamber and other warm components of the system with the cryogenic fuel. Figure 15

The architecture of the blow-down tank has been selected in accordance with the propellant used for each tank.

For the RP1 fuel it was decided to use a bladder tank, similar to the one developed by the Ariane group for the hydrazine Attitude and Orbital Control System (AOCS) of all versions of Ariane 5 [23]. This tank can be implemented in a RP1 system as the chemical corrosion of the fuel is significantly lower than hydrazine. The tank is composed of spherical bladder placed inside the tank, where the pressurizing gas is placed on the outside compressing the fuel placed inside and forcing it to exit the tank. As mentioned in subsection 2.9, the feeding line of the oxidizer passes through the centre of the tank; this is done for two main reasons: to shorten the length of the oxidizer feeding line, thus reducing pressure losses, and to provide an anti-sloshing solution for the fuel inside the tank during the movement of the spacecraft.

While for the LOX tank a different architecture was used to accommodate for the chemical and corrosive properties of the cryogenic oxidizer. While a simple and reliable solution commonly used is a piston architecture, this was discarded due to the large D/L ratio of the tank, which would result in an excessively large piston. For this reason, a metal bladder was chosen as the blow-down architecture of the system, as it has been demonstrated to be the best bladder choice for cryogenic propellants. [41]

As a preliminary choice for a pressurizing gas, it has been chosen to use helium as inert gas as allows to obtain a lower final pressurizing gas temperature in the tank. As per design the pressurizing gas will be collocated in the same tank as the fuel and oxidizer.

The sizing of the tanks is approached by starting from the available volume percentage decided for the mission, from the 80% of the total space, as per requirement, the volume of the chamber and of the convergent were removed to assign all the remaining volume for the tanks. The approach adopted involves allocating the space according to the volume OF ratio and assuming a maximum pressure drop of 30 bar in the combustion chamber, which occurs in the worst scenario allowed. To compute the actual volume of fuel and oxidizer in the tanks the amount of Helium in both tanks has to be computed before. To evaluate it, the adiabatic expansion solution was applied. The fuel volume is found by solving this system of equations:

$$\begin{cases} V_{tot} = V_{ox} + V_f + V_{He_{ox},1} + V_{He_f,1} \\ V_{He_f,1} = (V_f + V_{He_f,1}) \left( \frac{P_{f,2}}{P_{f,1}} \right)^{1/\gamma_{He}} \\ V_{He_{ox},1} = (V_{ox} + V_{He_{ox},1}) \left( \frac{P_{ox,2}}{P_{ox,1}} \right)^{1/\gamma_{He}} \\ V_{ox} = OF \cdot V_f \end{cases} \quad (24)$$

After the volumes are obtained, the height of the tanks was easily computed. Knowing the volume of both the propellants, and by considering an ullage margin of 2 %, the propellant mass is obtained. To compute the thickness of the Aluminium walls of the tank a 100 % margin is considered to obtain the burst pressure from the tanks pressure and then, by knowing the ultimate tensile strength  $\sigma = 350\text{MPa}$ , it is possible to obtain the thickness:

$$t_{tank} = \frac{P_{burst} D_{tank}}{2\sigma} \quad (25)$$

Finally, the masses of the tanks' shells are computed knowing the total area and the thickness. Knowing the molar mass of He, the actual density of the pressurizing gas can be easily evaluated and from the volume of the two tanks the Helium mass is finally computed.

### 3 Simulation

A simulation has been done to analyze the performance of the engine during the whole firing, the simulation runs on 10 s time steps. The general structure of the program can be seen in Figure 1.

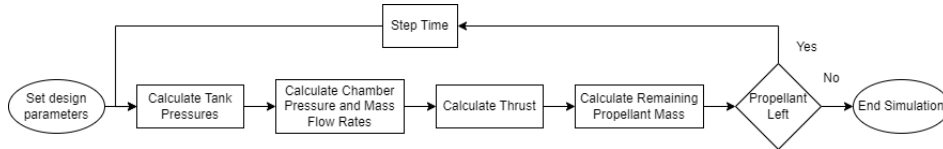


Fig. 1: Simulation program structure

#### 3.1 Tank Pressures

The expansion of the pressurant gas in the tanks is considered adiabatic. The pressure in the tanks is calculated with the following formula:

$$P_{ox} = P_{i,ox} \cdot \left( \frac{V_{t,ox} - \frac{m_{i,ox}}{\rho_{ox}}}{V_{t,ox} - \frac{m_{ox}}{\rho_{ox}}} \right)^\gamma \quad P_{fu} = P_{i,fu} \cdot \left( \frac{V_{t,fu} - \frac{m_{i,fu}}{\rho_{fu}}}{V_{t,fu} - \frac{m_{fu}}{\rho_{fu}}} \right)^\gamma \quad (26)$$

With  $P_i$  the initial tank pressure,  $V_t$  the volume of the tank,  $m_i$  the initial mass of propellant,  $m$  the current mass of propellant, and  $\rho$  the density of the propellant.

## 3.2 Chamber Pressure and Mass Flow Rates

The chamber pressure and mass flow rate are calculated with an iterative function, for the initial estimates it uses the chamber pressure and mass flow rate calculated in the previous time step. The function continues iterating until it detects the convergence of the values of the chamber pressure and mass flow rates. The function has the structure seen in Figure 21.

### 3.2.1 Engine Discretization

To calculate the pressure losses in the engine cooling jacket, the cooling of its walls and the heating of the propellant, it is discretized into 100 straight tubular sections. The structure is characterized by a straight combustion chamber, an RAO convergent up to  $45^\circ$  where it becomes conical, and an RAO divergent [15]. The various sections are allocated as follows in order to maximize resolution where it's most critical: 15% to the combustion chamber, 45% to the throat, and 40% to the nozzle.

### 3.2.2 Engine Cooling Jacket

The cooling jacket is divided into 4 sectors: the chamber, the nozzle, the hot divergent and the cold divergent. The cold divergent being the part of the divergent where the gasses are colder than the maximum service temperature of the material, such that it doesn't require cooling. The cooling jacket is composed of repeating up-and-down pipes in order to increase the fluid's velocity, by reducing the entry and exit areas, and keeping the same heat exchange surface as only up pipes. Both the amount of times the fuel goes up and down as well as the width of the jacket varies on each sector.

The fuel path in the cooling jacket is:

1. It enters at the bottom part of the throat, where the jacket has a thickness of 1 mm and the fuel does a total of 9 passes;
2. Then it goes to the top of the hot divergent, where the jacket has a thickness of 3 mm and the fuel does a total of 5 passes;
3. Finally it gets into the top of the chamber, where the jacket has a thickness of 3 mm and the fuel does a total of 6 passes and finishes at the injectors;

### 3.2.3 Pressure Losses

The pressure losses are the same as those analyzed in the nominal sizing section, however they are calculated at each time step. The pressure drop at the check valve is calculated for the estimated volumetric flow rates using the information from Figure 17. Also a more detailed analysis of the cooling jacket losses has been carried out: the friction factor is calculated in each section, taking into account the increase in velocity due to the number of passes the fuel makes.

In particular, it can be noted that for each section of the jacket, when the Reynolds number is greater than 4000, the friction factor is calculated using the Equation 18 with the corrected Reynolds number and the relative roughness for concentric tubes using the correction factor table provided in Table 18. While if the Reynolds number is less than 2300, the flow is laminar, so the friction factor is calculated as  $f_n = \frac{64}{Re_n \cdot \epsilon_n}$ , with  $\epsilon_n$  being the correction factor taken from Table 18 for each section. Finally, if the Reynolds number is between 2300 and 4000, the flow is transitional, and due to the lack of a better model, the friction factor is linearly interpolated between laminar at 2300 and turbulent at 4000. The total friction losses in the nozzle are then calculated as:

$$F_{nozz} = \sum_{n=1}^{100} \frac{f_n \cdot L_n}{2D_h \cdot A_{jacket,n}^2} \quad (27)$$

### 3.2.4 Mass Flow Rate

To calculate the mass flow rates the displacement thickness on the nozzle was taken into account, and the  $Cd^*$  of the throat is calculated using Equation 11. Then the mass flow rates are calculated using the

Bernoulli equation with losses and the obtained formulas for the oxidizer and the fuel mass flow rates are:

$$\begin{aligned}\dot{m}_{calc,ox} &= Cd^* \cdot \sqrt{\rho_{ox} \cdot \frac{P_{ox} - P_{cc} - \Delta P_{check\ valve,ox}}{\frac{K_{CD}}{2A_{inj,ox}} + \frac{1+K_{entry}+K_{valve}+f_{D,ox} \cdot \frac{L_{feed,ox}}{D_{feed,ox}}}{2A_{feed}^2}}} \\ \dot{m}_{calc,fu} &= Cd^* \cdot \sqrt{\rho_{fu} \cdot \frac{P_{fu} - P_{cc} - \Delta P_{check\ valve,fu}}{\frac{K_{CD}}{2A_{inj,fu}} + \frac{1+K_{entry}+K_{valve}+f_{D,fu} \cdot \frac{L_{feed,fu}}{D_{feed,fu}}}{2A_{feed}^2} + F_{nozz}}}\end{aligned}\quad (28)$$

However to make the iterative scheme more stable the mass flow rates are taken as the average of the calculated mass flow rates and the estimated mass flow rates:

$$\dot{m}_{ox} = \frac{\dot{m}_{calc,ox} + \dot{m}_{est,ox}}{2} \quad \dot{m}_{fu} = \frac{\dot{m}_{calc,fu} + \dot{m}_{est,fu}}{2} \quad (29)$$

### 3.2.5 Regenerative Cooling

The regenerative cooling is calculated with an iterative function, for the initial estimates it uses the fuel and wall temperature from the previous time step. The function continues iterating until it detects the convergence of the fuel and wall temperature. The function has the structure seen in Figure 22.

First the chamber properties  $\gamma$ ,  $T_{chamb}$  and  $c_{star}$  are calculated using the NASA CEA code, considering the oxidizer fuel ratio obtained from the mass flow rates, the estimated combustion chamber pressure and estimated temperature of the fuel.

Then the Mach number is calculated at each  $n$  section of the chamber, solving the following equation for Quasi-1D isentropic flow:

$$A_t = \frac{1}{M_n} \frac{2}{\gamma + 1} \left(1 + \frac{\gamma - 1}{2} M_n^2\right)^{\frac{\gamma + 1}{2(\gamma - 1)}} \quad (30)$$

Then the temperature and pressure can be calculated in each section with the following formulas:

$$T_{gas,n} = T_c \left(1 + \frac{\gamma - 1}{2} M_n^2\right)^{-1} \quad (31) \quad P_{gas,n} = P_c \left(1 + \frac{\gamma - 1}{2} M_n^2\right)^{-\frac{\gamma}{\gamma - 1}} \quad (32)$$

The Bartz correlation for calculating the heat transfer coefficient inside rocket engines, detailed by [24], requires that the gas properties be calculated at a specific temperature  $T_{star}$  that is calculated with the following formula:

$$T_n^* = T_{gas,n} \left(1 + 0.032 M_n^2 + 0.58 \frac{T_{wall,n}}{T_{gas,n} - 1}\right) \quad (33)$$

The Prandtl ( $Pr$ ), dynamic viscosity ( $\mu$ ) and specific heat ( $Cp$ ) can be calculated for each  $n$  section with the NASA CEA code using the Temperature/Pressure mode by giving it the  $T_n^*$  and  $P_{gas,n}$  at each section.

Following the Bartz correlation [24] the  $h_{gas}$  of each section is calculated using the following formula:

$$h_{gas,n} = \frac{0.026}{D^{*0.2}} \left(\frac{\mu_n^{0.2} \cdot Cp_n}{Pr_n^{0.6}}\right) \cdot \left(\frac{P_{cc}}{c^*}\right)^{0.8} \cdot \left(\frac{D^*}{2 \cdot k_t}\right)^{0.1} \cdot \left(\frac{A^*}{A_n}\right)^{0.9} \cdot \sigma_n \quad (34)$$

Where  $\sigma$  is defined as:

$$\sigma_n = \frac{1}{\left[\frac{1}{2} \frac{T_{w,n}}{T_0} \left(1 + \frac{\gamma - 1}{2} M_n^2\right) + \frac{1}{2}\right]^{0.68} \cdot \left[1 + \frac{\gamma - 1}{2} M_n^2\right]^{0.12}} \quad (35)$$

Next, it is necessary to calculate the convection in the cooling jacket. For this, 3 possibilities are considered. If the Reynolds is smaller than 2300 the flow is laminar and the laminar Nusselt number can be

obtained from Table 19 as a function of the relation of internal and external diameter. If the Reynolds number is bigger than 4000 the Petukhov-Popov correlation [34] is used:

$$K1 = 1 + 3.4f_{Nozzle} \quad K2 = 11.7 + \frac{1.8}{Pr_{fu}^{\frac{1}{3}}} \quad (36)$$

$$Nu_{fu,n} = \frac{\frac{f_n}{8} \cdot Re_n Pr_{fu}}{K1 + K2 \cdot \left(\frac{f_n}{8}\right)^{0.5} \cdot \left(Pr^{\frac{2}{3}} - 1\right)} \quad h_{fu,n} = \frac{k_{fu}}{D_{h,n}} \cdot Nu_{fu,n} \quad (37)$$

Where  $f_n$  is the friction factor calculated in the cooling jacket.

In the case the Reynolds is between 2300 and 4000 the flow is transitional, and due to the lack of better models, the Nusselt number is linearly interpolated between laminar at 2300 and turbulent at 4000.

Then the heat transfer coefficient can be calculated for each section as:

$$U_n \cdot A_n = \frac{1}{\frac{1}{h_{gas,n} \cdot A_{int,n}} + \frac{1}{h_{fu,n} \cdot A_{ext,n}} + \frac{t_{wall}}{k_{wall} \cdot A_{avg,n}}} \quad (38)$$

With the surface area corrected for the number of channels:

$$A_{int,n} = \frac{L_n \cdot \pi \cdot d_n^2}{4 \cdot N_{channels}} \quad A_{ext,n} = \frac{L_n \cdot \pi \cdot d_n^2}{4 \cdot N_{channels}} \quad A_{avg,n} = \frac{A_{int,n} + A_{ext,n}}{2} \quad (39)$$

Now the fuel can be calculated as it cycles through each section. To calculate the heat transferred in each section, the logarithmic mean temperature difference is used with the following equation:

$$LMTD = \frac{T_{fu,out} - T_{fu,in}}{\log(T_{gas,n} - T_{fu,in}) - \log(T_{gas,n} - T_{fu,out})} \quad (40)$$

$$U_n \cdot A_n \cdot LMTD = \dot{m}_{fu} \cdot Cp_{fu} \cdot (T_{fu,out} - T_{fu,in})$$

This equation is solved throughout the journey of the fuel, including the up and down passes. Starting at the throat and doing 9 passes, then 5 passes in the nozzle and 6 passes in the chamber. The value of the temperature obtained at the end is the temperature of the fuel at the injector. For every pass the value of the heat flow is calculated and it's added to the total heat flow of that section:

$$q_n = q_n + \dot{m}_{fu} \cdot Cp_{fu} \cdot (T_{fu,out} - T_{fu,in}) \quad (41)$$

Then the temperature of the wall at each section can be calculated as:

$$T_{wall,n} = T_{gas,n} - \frac{q_n}{A_{int,n} \cdot h_{gas,n}} \quad (42)$$

Finally convergence of 1% is checked between the current and previous estimation of fuel and wall temperature.

This model is quite limited as it only considers heat flow in the wall in the radial direction, in reality it's expected that the wall also conducts heat in the axial direction. However this would have an effect of averaging the temperature and cooling hot spots. A more sophisticated 3D conduction model would be required for a detailed knowledge of the wall temperatures.

Another limitation of the model is that the properties of the fuel are considered constant. This is really not the case for the range of temperatures that the fuel experiences. The expected variation would be: a decrease of density of about 18%, a decrease of kinematic viscosity of about 70% and a decrease of thermal conductivity of about 27% [25]. This was not implemented into the simulation due to a lack of time, however it should be incorporated into any follow ups of this work.

### 3.2.6 Chamber Properties and Pressure

The  $\gamma$ ,  $T_{cc}$ ,  $R_{gas}$  and  $Re_{throat}$  of the engine are calculated with the NASA CEA code, considering frozen reactions. The code is run using the OF ratio obtained with the calculated mass flow rates, the estimated chamber pressure and the fuel temperature.

Then the chamber pressure is calculated with the following formula:

$$P_{calc,cc} = \frac{(\dot{m}_{fu} + \dot{m}_{ox})}{A^*} \cdot \sqrt{\frac{T_{cc} \cdot R}{\gamma}} \cdot \left(\frac{\gamma + 1}{2}\right)^{\frac{\gamma+1}{2(\gamma-1)}} \quad (43)$$

However to make the iterative scheme more stable the chamber pressure is taken as the average of the calculated chamber pressure and the estimated chamber pressure:

$$P_{cc} = \frac{P_{calc,cc} + P_{est,cc}}{2} \quad (44)$$

Finally the function checks for convergence of 0.01% of the previous and current mass flow rates and chamber pressure.

### 3.3 Thrust

The exit pressure of the engine is calculated by solving Equation 2, considering the calculated chamber pressure and gamma.

Then the 2D losses are calculated using Equation 9 and the  $C_t$  can be calculated as:

$$c_t = \lambda \cdot \sqrt{\frac{2\gamma^2}{\gamma-1} \left(\frac{2}{\gamma+1}\right)^{\frac{\gamma+1}{\gamma-1}} \left(1 - \left(\frac{P_e}{P_{cc}}\right)^{\frac{\gamma-1}{\gamma}}\right)} + \frac{P_e}{P_{cc}} \epsilon \quad (45)$$

Finally the thrust is calculated as:

$$T = P_{cc} \cdot A^* \cdot c_t \quad (46)$$

### 3.4 Remaining Propellant Mass

The remaining propellant mass is calculated considering a constant mass flow rate during the time step, then:

$$m_{ox} = m_{ox} - \dot{m}_{ox} \cdot \Delta t \quad m_{fu} = m_{fu} - \dot{m}_{fu} \cdot \Delta t \quad (47)$$

The program runs the next time step until it detects that either the mass of fuel or oxidizer falls below 3% of the initial fuel and oxidizer mass. This is to account for ullage and leftover propellant in the pipes.

## 4 Results and Comments of the Nominal Design

### 4.1 Nozzle

#### 4.1.1 Expansion Ratio Choice [2.3.1]

The maximum achievable change in velocity,  $\Delta v$ , is obtained at an expansion ratio of  $\epsilon = 65$ . This is attributed to the fact that while the specific impulse ( $I_{sp}$ ) increases, so does the mass of the nozzle. This trend continues until a configuration is reached where the increase in  $I_{sp}$  no longer compensates for the increase in mass. This result aligns with values observed in operational spacecraft and is further justified by the choice of material. Specifically, C-103 is a dense niobium-based alloy with a density of  $\rho_{C-103} = 8470 \text{ kg m}^{-3}$ . It is the high density of the material that constrains the enhancement in performance for larger values of  $\epsilon$ .

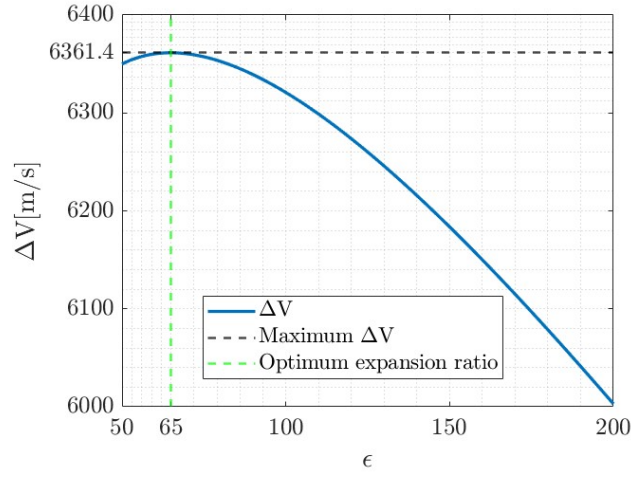


Fig. 2:  $\Delta V$  as a function of  $\epsilon$

Additionally, commercially available additive manufacturing dimensions are limited to  $420 \times 275 \times 275$  mm [8][3]. With  $\epsilon = 65$  the obtained total length of the thrust chamber  $l_{tc}$  is 292.2 mm and the exit diameter  $d_e$  is 93.9 mm. Both dimensions are suitable for additive manufacturing applications.

#### 4.1.2 General Nozzle Dimensioning Parameters [2.3.2]

The values obtained for the dimensioning of the nozzle are the following:

Table 6: Nozzle parameters

Parameter	Value	Parameter	Value
$P_e$	4746 Pa	$d_e$	0.0939 m
$c^*$	1774.4 m s <sup>-1</sup>	$I_{sp}$	339.4 s
$c_t$	1.8762	$m_{flow}$	0.300 kg s <sup>-1</sup>
$d_t$	0.0117 m	$v_e$	3219.8 m s <sup>-1</sup>

The near vacuum exit pressure is coherent with the design request of vacuum operating conditions. The  $c^*$ ,  $c_t$ ,  $I_{sp}$ , and  $v_e$  are in line with highly efficient LOX RP1 applications in vacuum. These parameters are similar to those observed in the Rocket Lab Electron, which is optimized for efficiency in small satellite launches. The small throat and exit diameters, along with the low mass flow rate, are coherent with the low level of thrust required for the mission.

## 4.2 Combustion Chamber [2.4]

The results for the combustion chamber are as follows: These values reflect the small size of the engine.

Table 7: Combustion Chamber results

Parameter	Value
$V_{cc}$	$1.2184 \times 10^{-4} \text{ m}^3$
$\epsilon_c$	9 (rounded up)
$d_c$	0.035 m
$l_{cc}$	0.1270 m

With these dimensions, the critical factor will be cooling, since there is very little area available for heat exchange. The contraction ratio ( $\epsilon_c$ ) was rounded up to the upper integer to simplify the dimensioning and design.

### 4.3 Conical Nozzle [2.5]

The dimensions of the conical nozzle are as follows:

Table 8: Conical Nozzle results

Parameter	Value
Convergent half-angle ( $\alpha_c$ )	45°
Divergent half-angle ( $\alpha_d$ )	15°
Length of the convergent section ( $L_c$ )	0.0117 m
Length of the divergent section ( $L_d$ )	0.1535 m

These dimensions, obtained with a divergent half-angle of 15°, mark the beginning of the RAO nozzle computation.

### 4.4 RAO Nozzle [2.6]

The RAO nozzle for maximum performance has the following dimension:

Table 9: Dimensions of the RAO Nozzle

Parameter	Value
Initial RAO angle ( $\theta_{RAOi}$ )	40.18°
Exit RAO angle ( $\theta_{RAOf}$ )	4.13°
Length of the convergent section ( $L_c$ )	0.0117 m
Length of the divergent section ( $L_d$ )	0.1535 m

In comparison to the conical nozzle design, as detailed in the subsequent section on nozzle losses, using identical dimensions yields a more efficient nozzle with regard to 2D losses. The profile is shown in Figure 23

### 4.5 Nozzle Losses [2.7]

Regarding nozzle losses, the following results are obtained:

Table 10: Nozzle Losses

Parameter	Value
$\lambda_{RAO}$	0.9930
$C_d$	0.9845
$\dot{m}_{flow, real}$	0.2957 kg s <sup>-1</sup>
$T_{real}$	978.4 N
$T_{decrease\_perc}$	-2.16%
$I_{spReal}$	337.3 s

Both the divergent and viscosity losses are minimal, resulting in a thrust loss percentage of only -2.16%. This is attributed to the following factors:

- Divergence losses are minimized by using a RAO nozzle design. For conical nozzles, the loss coefficient ( $\lambda$ ) would be calculated as  $\lambda = \frac{1+\cos(\alpha_d)}{2} = 0.983$ , resulting in a total thrust loss percentage of -3.12%. Therefore, the RAO design saves nearly 1% in thrust loss.
- The mass flow loss due to viscosity effects is estimated at -1.55%, which aligns with typical values reported in Rocket Propulsion Elements.



Finally the real specific impulse reflects correctly a little decrease (-0.62%) in the performance compared to the ideal one.

#### 4.6 Injectors [2.8]

	$v[m\ s^{-1}]$	$\Delta P[bar]$
<b>LOX</b>	23.42	6.36
<b>RP-1</b>	24.69	5.99

Table 11: Injection Plate results

The computed pressure drop with the selected configuration are 12.72% for the oxidizer and 11.98% for the fuel. The results can be considered meaningful as reflected by the correspondence with usual pressure drops in similar applications where estimated values stand between 5-15%. Such values are required for:

- **Efficient Mixing:** a higher pressure drop ensures that the propellants are adequately atomized and mixed before entering the combustion chamber, leading to more efficient combustion and higher thrust;
- **Thermal Management:** by controlling the pressure drop across the injection plate, the mass flow rate can be regulated and this will help to manage the combustion;
- **Chugging Problem:** a greater injector pressure drop, that tends to make chamber pressure oscillations small relative to delivery pressure, decreases chugging;[37]

The velocity of injection of propellant couple demonstrates the fairness of the plate sizing since it's restrained between the typical values 10-50  $m\ s^{-1}$ .

#### 4.7 Feeding Line [2.9]

	<b>LOX</b>	<b>RP-1</b>
$\Delta P_{feed}$	0.461	0.084
$\Delta P_{dyn}$	0.234	0.055
$\Delta P_{check\ valve}$	2.5	2.5
$\Delta P_{entry}$	0.12	0.028
$\Delta P_{sol\ valve}$	0.064	0.018
$\Delta P_{cooling}$	0	0.015

Table 12: Pressure drops in bar

<b>LOX</b>	<b>RP-1</b>
60.32	58.99

Table 13: Tanks Pressure in bar

Considering all the pressure drops, the total pressure losses are 20.74%(oxidizer) and 17.98%(fuel) with respect to the combustion chamber pressure which are acceptable values for a rocket engine.

#### 4.8 Insulating Material [2.10]

The minimum thickness of the insulating material is equal to 3.7 mm which led to an insulant radius of 8.8 mm

Supposing a thickness of the stainless steel tube of 2 mm the insulant thickness is a reasonable value since the  $\Delta T$  that is required to be maintained is not that high and the selected material is specifically used for cryogenic applications with the liquid oxygen.

## 4.9 Tanks [2.11]

	LOX	RP-1
$L_{tank} [m]$	1.135	0.583
$M_{prop} [kg]$	270.60	120.80
$t_{tank} [cm]$	1.66	1.63
$M_{shell} [kg]$	226.71	146.06
$M_{He} [kg]$	5.43	2.69
$V_{tot,tank} [m^3]$	0.83	0.43
$Ullage_{Vol} [\%]$	66.08	65.17

Table 14: Tanks size

The lengths obtained for the two tanks optimize the available space, in fact the summation of these ones with the length of the combustion chamber and the convergent part of the engine lead to 1.84 m which is near the maximum length of 2 m. In this way the available space is used to allocate the system maintaining a certain margin between the two tanks and between fuel and combustion chamber permitting the insertion of the pipelines and valves.

The propellant couple masses respect the O/F ratio showing that oxidizer is around two times the fuel in the tanks while the Helium mass is much smaller. The use of Aluminium requires a significant thickness which lead to a great mass of the tanks' shells.

## 5 Results and Comments of the Simulation

### 5.1 Re-Sizing

Trough many simulations the nominal values have been slightly altered to optimize the ISP and OF ratio, and to get the correct initial thrust, initial chamber pressure and final chamber pressure.

The modified values for the system are:

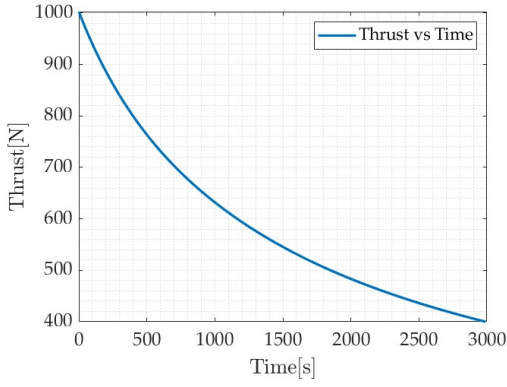
	Nominal	Re-Sized
$L_{tank,ox} [m]$	1.135	1.151
$L_{tank,fu} [m]$	0.583	0.567
$M_{ox} [kg]$	270.6	383.8
$M_{fu} [kg]$	120.8	159.9
$P_{ox} [bar]$	60.32	59.5
$P_{fu} [bar]$	58.99	61
$D_{inj,ox} [mm]$	1.2	1.2
$D_{inj,fu} [mm]$	1.2	1

Table 15: Caption

The change in size of the tanks was to get a better OF ratio. The increase in propellant mass was to get a lower final chamber pressure, as in the nominal design the pressure losses at the minimal chamber pressure were overestimated. The pressures in the tanks were changed to get a correct initial chamber pressure and OF ratio. The diameter of the fuel injector was changed to get a more consistent OF ratio during the duration of the burn.

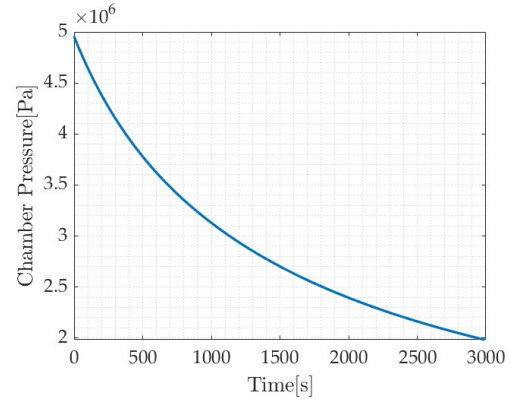
### 5.2 Results

The final burn time is of 2990s (59 minutes, 50 seconds), with an average thrust of 590.43N, a total impulse of 1.77e6Ns and an average specific impulse of 342.42s.



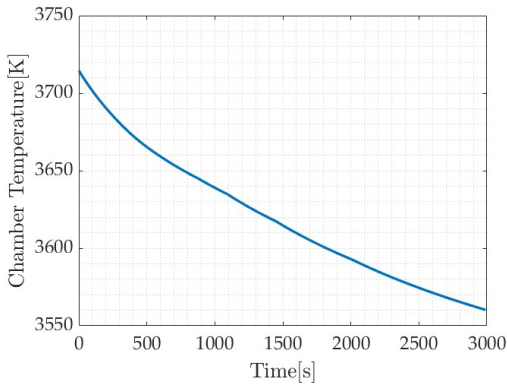
(a) Thrust vs Time

The initial thrust is  $1002.9N$ , within 1% error of the required  $1000N$ .



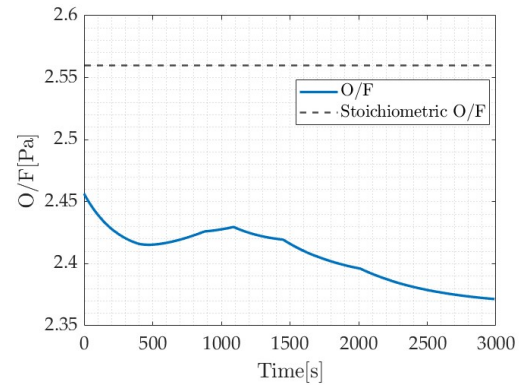
(b) Combustion Chamber Pressure vs Time

The initial and final chamber pressures are  $49.56bar$  and  $19.84bar$ , within 1% error of the required  $50bar$  and  $20bar$ .



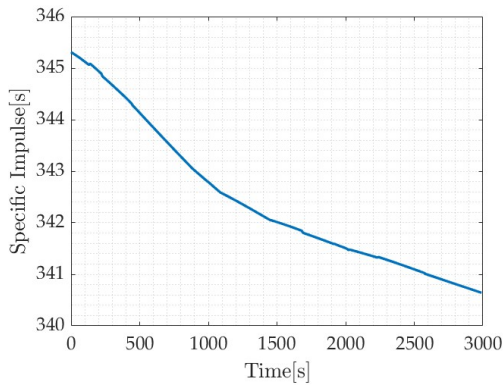
(a) Combustion Chamber Temperature vs Time

The chamber temperature decreases with time, this is due to the decrease in pressure that leads to an inefficient combustion.

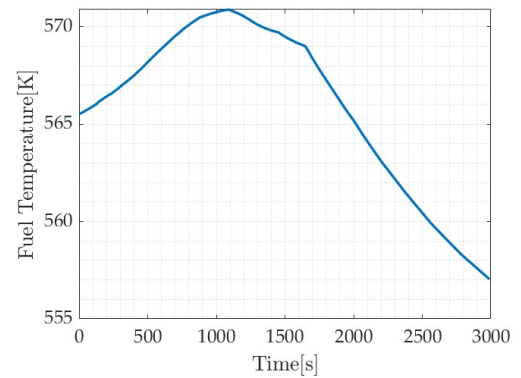


(b) O/F Ratio vs Time

The OF ratio is lower than the stoichiometric ratio, however the slightly fuel rich mixture has a better performance as it increases combustion temperature. The OF ratio only varies slightly during the burn.

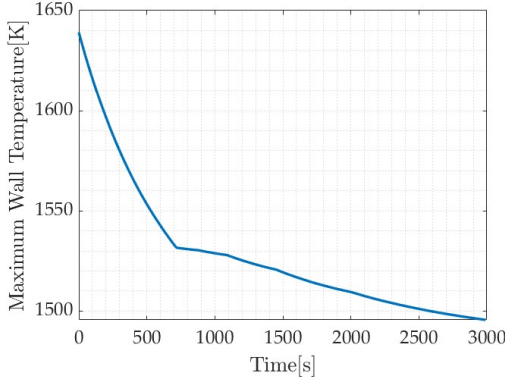


(a) Specific Impulse vs Time



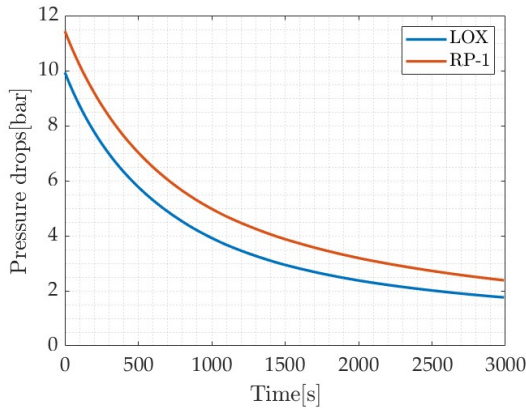
(b) Fuel Temperature vs Time

We managed to maintain an almost constant ISP throughout the burn, with only a variation of 1.35% from beginning to end. The slight decrease in ISP is due to the lowering of the chamber temperature.



(a) Max Wall Temperature vs Time

The temperature of the engine walls are kept below the maximum service temperature of 1753K [13] of the material throughout the whole burn.



(a) Pressure Drops vs Time

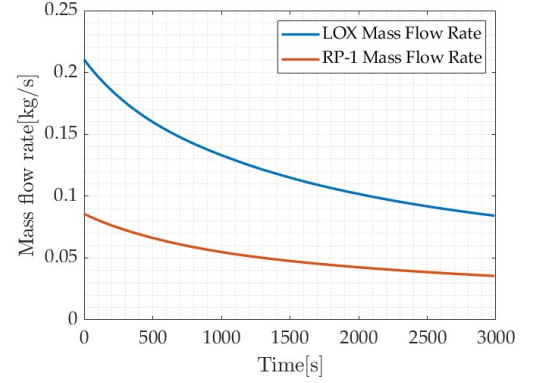
It can be seen how initially the pressure drop from the tanks is very high, however as the flow rate diminishes the pressure drop decreases significantly.

### 5.3 Off-Nominal Condition

The evaluation of the off-nominal condition is essential considering the tolerances associated with additive manufacturing. The chosen manufacturing process is LBPF, which leads to minimum tolerances of  $\pm 0.1$  mm. These tolerances primarily affect the injector holes. Indeed, due to their small diameters, the tolerances greatly change the injection area. This leads to relevant changes in mass flow rates entering the combustion chamber and therefore in engine performance.

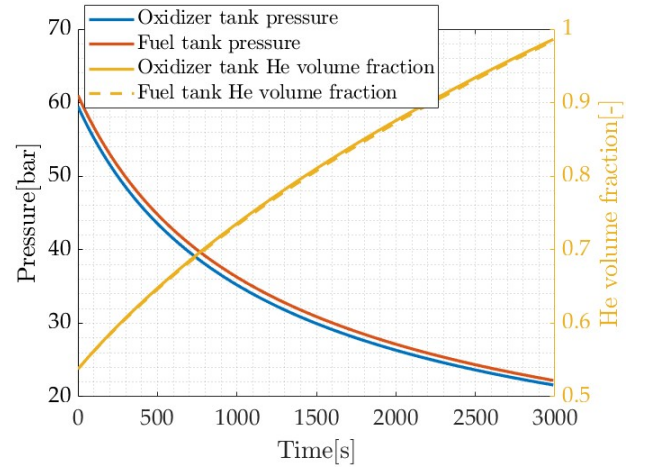
The analysis is conducted considering two limiting scenarios: one in which all hole diameters are increased by 0.1 mm, and the other in which they are all decreased.

The temperature of the fuel is kept below the critical temperature of RP-1 of 639 [25] throughout the whole burn.



(b) Mass Flow Rate vs Time

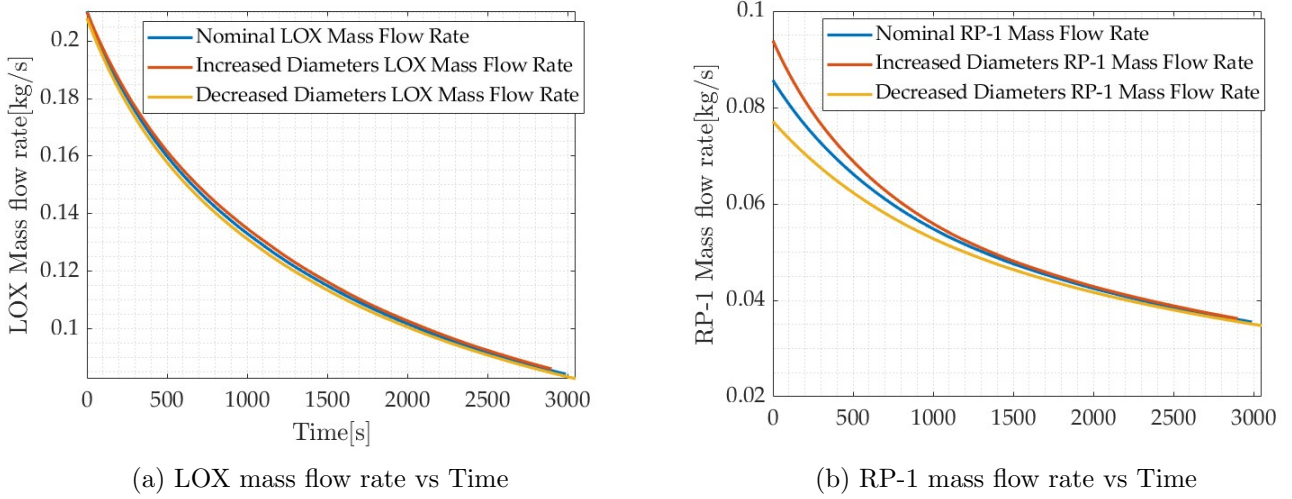
As expected the mass flow rate of both oxidizer and propellant diminishes as the tank pressure decreases.



(b) Tanks Pressure and Helium Volume Fraction vs Time

As the Tank pressure of both oxidizer and fuel decay with time, the Helium volume fraction in the tanks rises until it reaches a value near 100% of the tanks total volume.

The analysis then starts considering the variation in mass flows:



The positive tolerance correctly increases the mass flow rate while the negative tolerance decreases it. This modifies consequently the pressure in the combustion chamber and accordingly the thrust. Due to the different holes diameters between oxidizer and fuel the effect of tolerances is different. Especially this is worst for the fuel since it has smaller holes and bigger impact of tolerances, bringing to a greater mass flow rate change (respectively +9.6% and -9.95% for the two cases while for LOX are much smaller) . This latter difference leads also to a change in the OF ratio. Therefore, both the pressure and OF ratio are modified, and with them the engine performances. As the time pass, the  $\Delta P$  diminishes and therefore also the difference of mass flow rate between the three cases.

$$\Delta \dot{m} = C_d \sqrt{\rho} \left( A_{tol} \sqrt{2\Delta P_{tol}} - A_{nom} \sqrt{2\Delta P_{nom}} \right) \quad (48)$$

The overall effect is a convergence of performances of the three cases analysed, also for all the parameters investigated below.

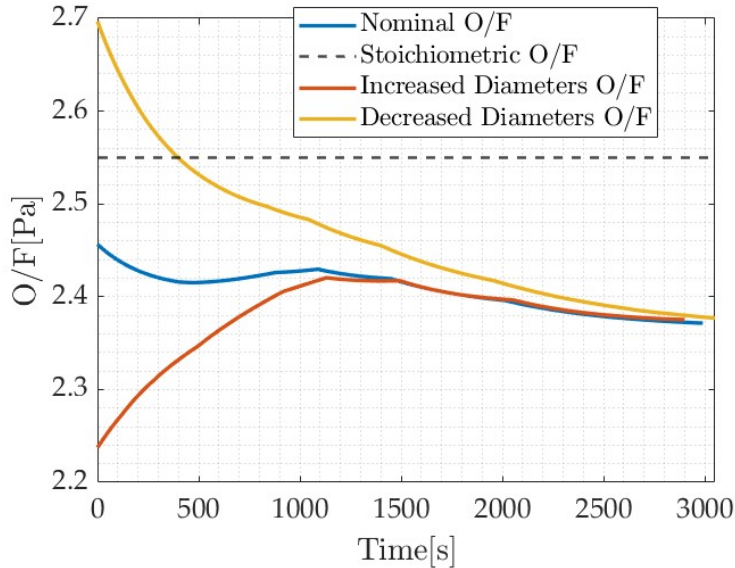
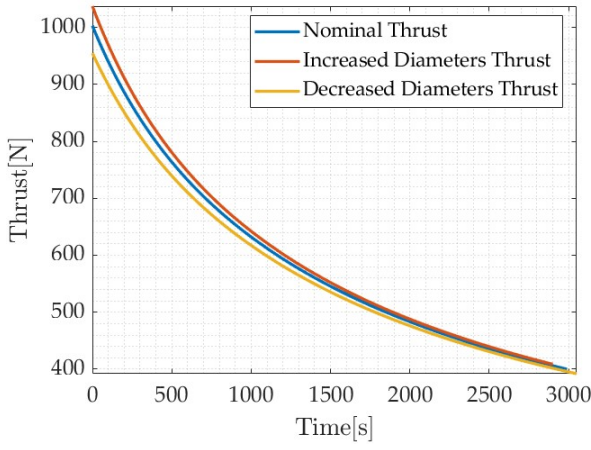
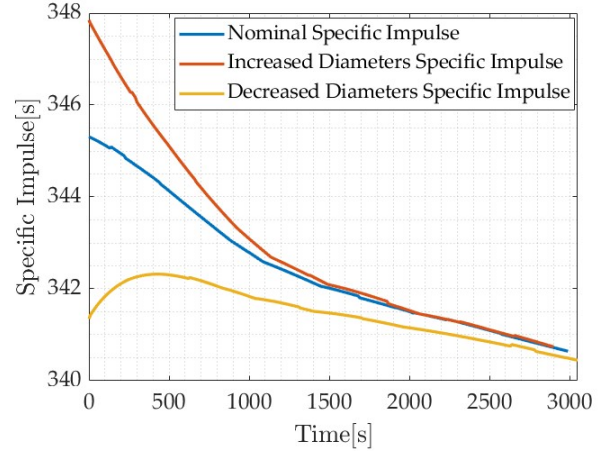


Fig. 9: OF ratio vs Time

As can be seen from the graph, the trend of the OF ratio follows the one stated in the mass flow rate analysis.



(a) Thrust vs Time



(b)  $I_{sp}$  vs Time

Both the thrust and  $I_{sp}$  follow the mass flow trend, increasing for enlarged holes (+3.42%) and decreasing for reduced ones (-4.79%). These are due to different reasons. The thrust, being a function of mass flow rate, correctly rises and decreases for the respective cases. On the other hand, the specific impulse becomes greater due to a change in OF ratio. Indeed, the OF ratio for a +0.1 mm is nearer to 2.24, which is the best one for LOX RP-1 applications considering the frozen expansion model in CEA analysis. The real optimal OF is higher than the frozen one, that is the reason behind the choice of OF=2.4 in the nominal simulation design. Instead, the -0.1 mm case moves further away from the optimum frozen condition, decreasing the performances. Therefore, this result is linked to the expansion model decided. Other noticeable tolerance effects are:

- Change in pressure: Particularly notable is the exceedance of 50 bar for the +0.1 mm case. This is not particularly harmful since the combustion chamber walls were primarily designed to resist thermal stresses. Instead, it contributes to the thrust increase.
- Change in wall temperature: This is critical for the -0.1 mm case. The limit operational temperature of C-103 is  $T_{wall} = 1753K$  [13]. The decrease in fuel mass flow rate reduces the cooling of the thrust chamber walls, resulting in the throat wall temperature becoming  $T_{wall} = 1650K$ , closer to the critical temperature ( $T_{wall} = 1635K$  for the nominal case).

## 5.4 Limitations of the model

The presented model has many limitations:

- Friction losses in the nozzle: the current model considers an isentropic nozzle with no friction.
- Heat losses in the nozzle: the current model does not account for the heat that is transferred to the fuel.
- Concentrated pressure drops in the cooling jacket: although the distributed pressure drops in the cooling jacket are considered, all the bends required to redirect the flow up and down would cause a pressure drop that we don't account for.
- Fuel properties: we consider the properties of the fuel constant with temperature.
- Engine wall temperature: a 3D heat transfer model would be required to accurately calculate the temperatures in the engine wall.
- Pressurant temperature: we consider the pressurant expansion as adiabatic, however with such a long burn that estimation is inaccurate.

However, we still consider that the model is accurate enough for a preliminary design of an engine, and that the real behaviour of such an engine would not deviate too much from our model.

## 6 Conclusion

The work done can be summarized in these main points:

- **Literature analysis on nozzle losses** [1.1]: Identify the main nozzle losses of liquid propulsion engine.
- **Literature analysis on Additive Manufacturing (AM)** [1.2]: Evaluating the best possible AM processes and studying the main issues and materials;
- **Literature analysis on blow-down system**[1.3]: Identify main problems which occur in blow-down systems and select the best architecture for our specific mission.
- **Engine modeling**[2]: A material selection analysis was conducted, followed by the structuring of the engine component design, evaluating the losses that affect it and the types of nozzles considered.
- **Simulation**[3]: A simulation was conducted to analyze the engine's performance and refine the design.
- **Nominal design and results**: A critical analysis and a comment on the results obtained[4][5].

Following the analysis conducted in the report, it was concluded that: concerning the nozzle losses, the most significant ones are the losses due to divergence and those caused by viscosity; for additive manufacturing, the focus was evaluated to be on the PBF process, particularly on LPBF, noting how roughness and intrinsic limitations must be a fundamental element to consider in the design phase; from an analysis of the main characteristics of the blow-down architecture, the importance of the type and material to be used according to the propellants used and the engine performance requirements. It is also concluded the need to use He as pressurizing gas and bladder tank for the RP-1, while for the LOX a metal bladder architecture.

A possible project follow-up could be a test campaign to obtain experimental data to verify the feasibility of the implemented design. Additionally, further investigation into the additive manufacturing tolerances could be pursued.

When considering the engine's overall design, several key conclusions emerge:

- Cryogenic propellants can pose critical challenges for blow-down systems, necessitating thermal insulation between the pressurizing gas and the propellant.
- Tank dimensions and, consequently, propellant masses do not align closely with the required thrust, resulting in extended burning times and huge inert mass.
- Engine dimensions, particularly the throat area, play a pivotal role in regenerative cooling due to the limited surface area available for heat exchange.



## References

- [1] Accuracies or Tolerances in 3D Printing.  
<https://3faktor.com/en/2016/12/14/accuracies-or-tolerances-in-3d-printing/>.
- [2] AISI 316 Technical Data Sheet. Technical report, Acciai Terni.  
<https://www.acciaiterni.it/wp-content/uploads/2017/07/316-NEW.pdf>.
- [3] Certified C-103 (A).  
<https://www.3dsystems.com/sites/default/files/2023-12/3d-systems-certified-c-103a-mds-letter-us-reva-web.pdf>.
- [4] Certified GRCop-42 (A).  
<https://www.3dsystems.com/sites/default/files/2023-07/3d-systems-certified-grcop-42a-datasheet-usen-2023-07-14-a-web.pdf?ind=aerospace>.
- [5] Cryogenic Tanks for Space Applications. Technical report, Air Liquide.  
<https://forum.nasaspaceflight.com/index.php?action=dlattach;topic=30981.0;attach=1366207>.
- [6] Data Sheet for Alluminum 7020-T6.  
<https://www.matweb.com/search/DataSheet.aspx?MatGUIDc66e13c1d36445c29bb9f852ccf2da17ckck=1>.
- [7] Direct Metal Laser Sintering (DMLS) for Metal 3D Printing.  
<https://www.protolabs.com/en-gb/services/3d-printing/direct-metal-laser-sintering/>.
- [8] DMP Flex 350, DMP Flex 350 Dual and DMP Flex 350 Triple.  
<https://www.3dsystems.com/3d-printers/dmp-flex-350>.
- [9] Fluid-press s.p.a. check valve catalog.  
<https://www.fluidpress.it/file/Home/prodotti/allegati/D025-SCHEDA.pdf>.
- [10] For Durable Insulation of Cryogenic Equipment.  
<https://plastics-rubber.basf.com/global/en/performance-polymers/products/basotect/cryogenic>.
- [11] INCONEL® 718 Product Specifications.  
<https://www.protolabs.com/media/5ozel3mp/inconel-en-screen-aw.pdf>.
- [12] LaserForm Ni718 (A).  
<https://www.3dsystems.com/sites/default/files/2023-12/3d-systems-laserform-ni718a-mds-letter-us-revd-web.pdf>.
- [13] Niobium C-103 (WC 103; 89Nb-10Hf-1Ti).  
<https://www.matweb.com/search/datasheet.aspx?matguid=ccea95c1083240d49fad4525686007f5>.
- [14] Special Metals INCONEL® Alloy 718.  
<https://asm.matweb.com/search/SpecificMaterial.asp?bassnum=NINC34>.
- [15] The Thrust Optimised Parabolic nozzle.  
<http://www.aspirespace.org.uk/downloads/Thrustoptimisedparabolicnozzle.pdf>.
- [16] What is Direct Energy Deposition (DED)?  
<https://www.twi-global.com/technical-knowledge>.
- [17] What is Post-Processing in Additive Manufacturing?  
<https://www.postprocess.com/2022/09/what-is-post-processing-in-additive-manufacturing/>.
- [18] 6 Important Design Considerations for Metal 3D Printing, 2018. <https://amfg.ai/2018/05/24/6-design-considerations-for-metal-3d-printing/>.
- [19] What Metals Can You Print?, 2020.  
<https://www.digitalalloys.com/blog/what-metals-can-you-print/>.



- [20] Dr. David L. Ellis . Precipitate Size in GRCop-42 and GRCop-84 Cu-Cr-Nb Alloy Gas Atomized Powder and L-PBF Additive Manufactured Material .  
<https://www.researchgate.net/publication/366920744-Precipitate-Size-in-GRCop-42>.
- [21] A. J. Pavli. Design and Evaluation of High Performance Rocket Engine Injectors for Use with Hydrocarbon Fuels . Technical report, Lewis Research Center Cleveland, Ohio, 1979.
- [22] A. Terracciano, S. Carapellese, G. Bianchi, D. Liuzzi, M. Rudnykh, D. Drigo, F. Del Brusco. Additive Layer Manufacturing Technology In Avio Injector Head Design, 2017.  
<https://www.eucass.eu/doi/EUCASS2017-455.pdf>.
- [23] Ariane Space. Hydrazine Propellant Tanks Overview.  
<https://www.space-propulsion.com/spacecraft-propulsion/hydrazine-tanks/hydrazine-tank-overview.html>.
- [24] D. R. Bartz. Turbulent Boundary-Layer Heat Transfer from Rapidly Accelerating Flow of Rocket Combustion Cases and of Heated Air. Technical report, Jet Propulsion Laboratory. California Institute of Technology Pasadena. California, 1965.
- [25] Thomas J. Bruno. The Properties of RP-1 and RP-2. Technical report, National Institute of Standards and Technology.
- [26] Dr. David L. Ellis . Conductivity of GRCop-42 Alloy Enhanced .  
<https://ntrs.nasa.gov/api/citations/20050192166/downloads/20050192166.pdf>.
- [27] F. Kreith and R. M. Manglik and M. S. Bohn. *Principles of Heat Transfer*. Cengage Learning, 2011.
- [28] F. Maggi. Space Propulsion Course Notes.
- [29] Mark S. Bohn Frank Keith, Raj M. Manglik. *Principles of Heat Transfer, Seventh Edition*. Cengage Learning, 2010.
- [30] G. V. R. RAO. Exhaust Nozzle Contour for Optimum Thrust . Technical report, Marquardt Aircraft Co., Van Nuys, Calif. , 1958.
- [31] G.P. Sutton, O. Biblarz. *Rocket Propulsion Elements*. John Wiley & Sons Inc., 2017.
- [32] P. Gradl, S.E. Greene, C. Protz, B. Bullard, J. Buzzell, C. Garcia, J. Wood, K. Cooper, J. Hulka, and R. Osborne.  
Additive Manufacturing of Liquid Rocket Engine Combustion Devices: A Summary of Process Developments and Hot-Fire Testing Results, 2018.  
<https://ntrs.nasa.gov/api/citations/20180006344/downloads/20180006344.pdf>.
- [33] H.C. Hearn. Thruster Requirements and Concerns for Bipropellant Blowdown Systems. *Journal of Propulsion and Power*, 1988.  
<https://arc.aiaa.org/doi/abs/10.2514/3.23030?journalCode=jpp>.
- [34] C. B. Panchal J. J. Lorenz, D. T. Yung and G. E. Layton. An Assessment of Heat-Transfer Correlations for Turbulent Water Flow through a Pipe at Prandtl Numbers of 6.0 and 11.6. Technical report, Ocean Thermal Energy Conversion Program, Argonne National Laboratory, 1982.
- [35] J. Posada and M. Kwon. Topic 6: Injector Design.  
<https://wikis.mit.edu/confluence/display/RocketTeam/Topic+6>
- [36] NASA Technology Transfer Program. A One-piece Liquid Rocket Thrust Chamber Assembly.  
<https://technology.nasa.gov/patent/MFS-TOPS-93>.
- [37] P. Hill, C. Peterson. *Mechanics and Thermodynamics of Propulsion*. Pearson, 2014.
- [38] R. Humble. *Space Propulsion Analysis and Design*. Learning Solutions, 1992.

- [39] S. A. Leadbetter and H. W. Leonard, and E. J. Brock, Jr. Design and Fabrication Considerations for a I/Io-Scale Replica Model of the Apollo/Saturn V. Technical report, Langley Research Center Langley Station, Hampton, Va. , 1967.
- [40] Space X. Falcon 1 press kit, 2008.  
<https://web.archive.org/web/20081001161901/http://www.spacex.com/>.
- [41] J.A. Stark, M.H. Blatt, K.R. Burton, J.R. Elliott, E.H. Bock, and J. M. Haze. Study of Low Gravity Propellant Transfer. Technical report, Convair Aerospace Division of General Dynamics, 1972.  
<https://ntrs.nasa.gov/api/citations/19730005037/downloads/19730005037.pdf>.
- [42] T.W. Teasley, C.S. Protz, A.P. Larkey, B.B. Williams, P.R. Gradl.  
Design Optimization of High Performance Additively Manufactured Rocket Engine Injectors, 2021.
- [43] Frank M. White. *Fluid Mechanics, Fourth Edition*. McGraw-Hill, 1998.

A Appendix: Literature Analysis

Industry Materials developed for L-PBF, E-PBF, and DED processes *(not fully inclusive)*

<b>Ni-Base</b> Inconel 625 Inconel 718 Hastelloy-X Haynes 230 Haynes 282 Haynes 188 Monel K-500 C276 Rene 80 Waspalloy	<b>Al-Base</b> AlSi10Mg A205 F357 6061 / 4047	<b>Ti-Base</b> Ti6Al4V γ-TiAl Ti-6-2-4-2	<b>Bimetallic</b> GRCoP-84/IN625 C-18150/IN625
<b>Cu-Base</b> GRCoP-84 GRCoP-42 C-18150 C-18200 Gildcop CU110	<b>Fe-Base</b> SS 17-4PH SS 15-5 GP1 SS 304 SS 316L SS 420 Tool Steel (4140/4340) Invar 36 SS347 JBK-75 NASA HR-1	<b>Co-Base</b> CoCr Stellite 6, 21, 31	<b>MMC</b> Al-base Fe-base Ni-base
		<b>Refractory</b> W W-25Re Mo Mo-41Re Mo-47.5Re C-103 Ta	

Fig. 11: Printable materials used in space applications [42]

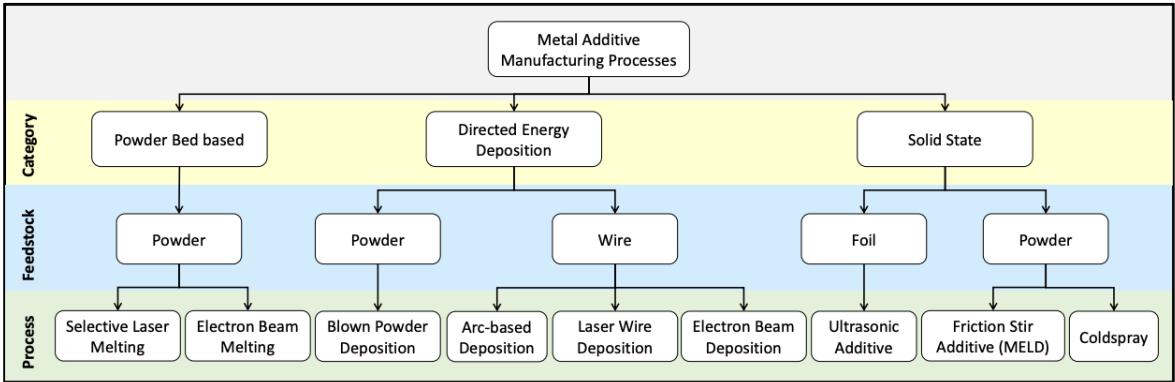


Fig. 12: AM processes1.2

## B Appendix: Engine Modelling

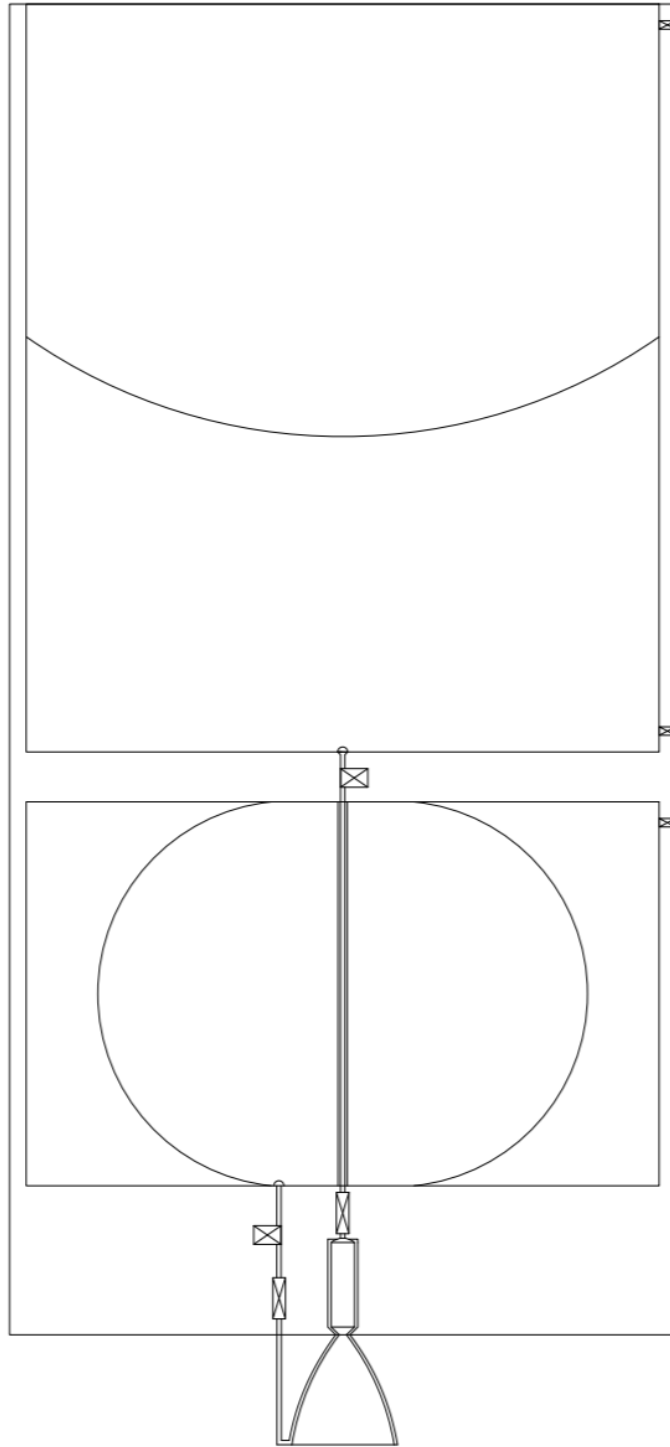


Fig. 13: CAD model

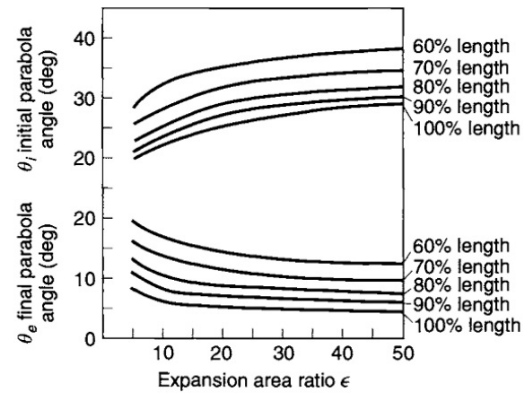


Fig. 14: RAO angles

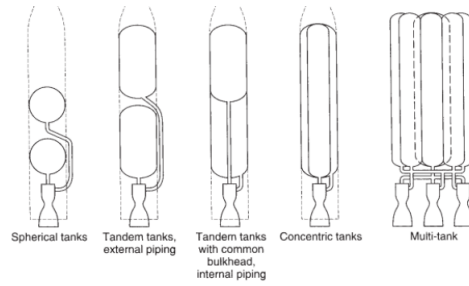


Fig. 15: Tandem tanks

Orifice Type	Diagram	Diameter (mm)	Discharge Coefficient
Sharp-edged orifice		Above 2.5	0.61
		Below 2.5	0.65 approx.
Short tube with rounded entrance $L/D > 3.0$		1.00	0.88
		1.57	0.90
		1.00	
		(with $L/D \sim 1.0$ )	0.70
Short tube with conical entrance		0.50	0.7
		1.00	0.82
		1.57	0.76
		2.54	0.84-0.80
		3.18	0.84-0.78
Short tube with spiral effect		1.0-6.4	0.2-0.55
Sharp-edged cone		1.00	0.70-0.69
		1.57	0.72

Fig. 16: Injectors types

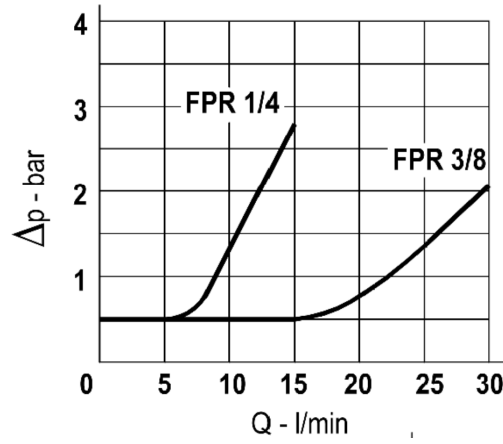


Fig. 17: Check valve pressure drop [9]

**Table 6.3** Laminar Friction Factors for a Concentric Annulus

$b/a$	$f Re_{D_h}$	$D_{eff}/D_h = 1/\zeta$
0.0	64.0	1.000
0.00001	70.09	0.913
0.0001	71.78	0.892
0.001	74.68	0.857
0.01	80.11	0.799
0.05	86.27	0.742
0.1	89.37	0.716
0.2	92.35	0.693
0.4	94.71	0.676
0.6	95.59	0.670
0.8	95.92	0.667
1.0	96.0	0.667

Fig. 18: Concentric tubes friction factor [43]

**TABLE 6.2** Nusselt number and friction factor for fully developed laminar flow in an annulus<sup>a</sup>

$\frac{D_i}{D_o}$	$\overline{Nu}_i$	$\overline{Nu}_o$	$f Re_{D_h}$
0.00	—	3.66	64.00
0.05	17.46	4.06	86.24
0.10	11.56	4.11	89.36
0.25	7.37	4.23	93.08
0.50	5.74	4.43	95.12
1.00	4.86	4.86	96.00

<sup>a</sup>One surface at constant temperature and the other insulated [13].

Fig. 19: Concentric tubes Nusselt number [29]

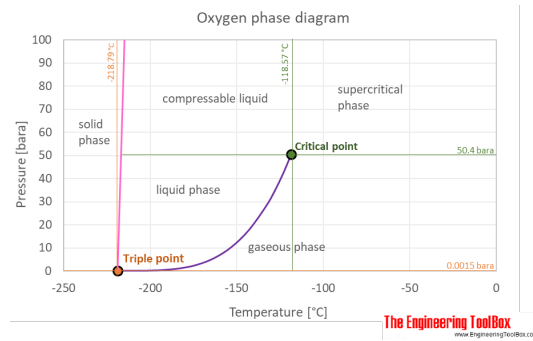


Fig. 20: LOX pressure with temperature [?]

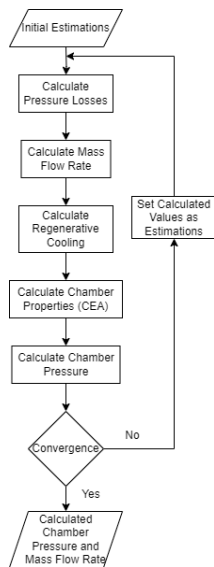


Fig. 21: Chamber pressure and mass flow rate function structure

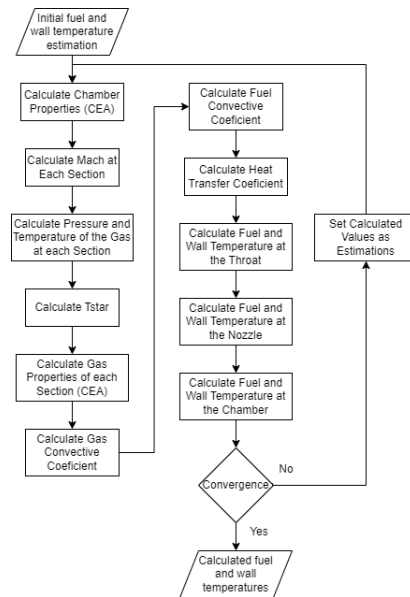


Fig. 22: Chamber pressure and mass flow rate function structure

## C Appendix: Results and Comments

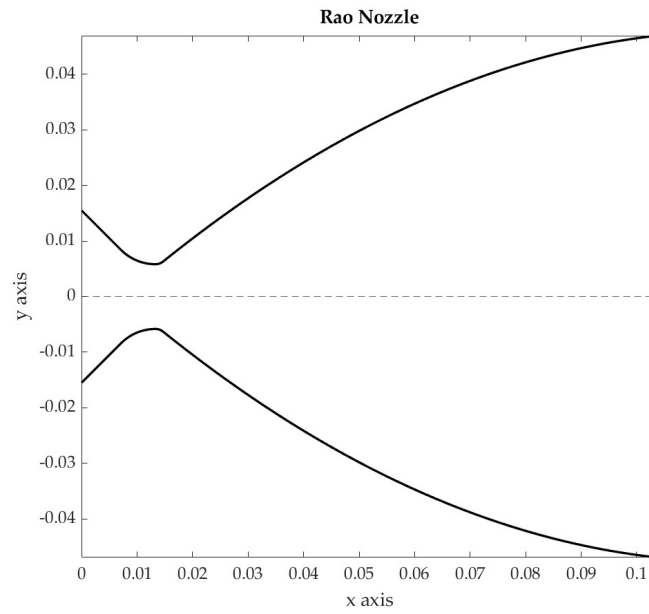


Fig. 23: Rao Nozzle profile